Natural speciation of Mn, Ni and Zn at the micrometer scale in a clayey paddy soil using X-ray fluorescence, absorption, and diffraction.

Alain Manceau, Caterina Tommaseo, Sophie Rihs, Nicolas Geoffroy, Daniel Chateigner, Michel Schlegel, Delphine Tisserand, Matthew A. Marcus, Nobumichi Tamura, Zueng-Sang Chen

Natural speciation of Mn, Ni and Zn at the micrometer scale in a clayey paddy soil using X-ray fluorescence, absorption, and diffraction

Alain Manceau[1,*], Caterina Tommaseo[1], Sophie Rihs[2], Nicolas Geoffroy[1], Daniel Chateigner[3], Michel Schlegel[4], Delphine Tisserand[1], Matthew A. Marcus[5], Nobumichi Tamura[5], Zueng-Sang Chen[6]

[1] Environmental Geochemistry Group, Maison des Géosciences, Univ. J. Fourier, BP 53, 38041 Grenoble Cedex 9, France.

[2] Centre de Géochimie de la Surface, Université Louis Pasteur, 1 rue Blessig, 67084 Strasbourg, France.

[3] CRISMAT-ENSICAEN, Bd. Maréchal Juin, 14050 Caen, France

[4] DEN/DPC/SCP, Centre d'études nucléaires de Saclay, BP 11, 91191 Gif sur Yvette, France

[5] Advanced Light Source, Lawrence Berkeley National Laboratory, One Cyclotron Road, Berkeley, California 94720, USA

[6] Department of Agricultural Chemistry, National Taiwan University, Taipei, Taiwan

Running Head: Mn, Ni and Zn speciation in soil

Index terms: speciation, heavy metal, Mn, Ni, Zn, soil, x-ray diffraction, XRD, x-ray fluorescence, SXRF, EXAFS spectroscopy, P-EXAFS, paddy soil.

* Author to whom correspondence should be addressed. E-mail: Alain.Manceau@ujf-grenoble.fr

ABSTRACT

The natural speciation of Mn (0.19 g/kg), Ni (46 mg/kg) and Zn (42 mg/kg) in the argillic horizon (120 cm depth, pH = 5.6) of an Ultisol from a paddy soil in northern Taiwan was investigated by advanced X-ray synchrotron techniques. Microchemical associations were imaged by synchrotron-based X-ray microfluorescence, host minerals were identified by standard and micrometer-resolved X-ray diffraction, and the local coordination environment of Mn, Ni, and Zn was probed using extended X-ray absorption fine structure (EXAFS) spectroscopy on a powdered sample and a soil thin section, and polarized EXAFS spectroscopy on a highly textured self-supporting clay film from the <2 μm fraction of the soil. Manganese was concentrated in Fe-Mn soft mottles (44.4 g/kg) as turbostratic hexagonal birnessite and lithiophorite having Mn^{3+}/Mn^{4+} atomic ratios of about 20 % and 50 %, respectively. Quantitative analysis of high order scattering paths of the EXAFS spectrum for natural and synthetic $(Al_{0.67}Li_{0.32})(Mn^{4+}_{0.68}Mn^{3+}_{0.32})O_2(OH)_2$ lithiophorite revealed that Mn^{3+} and Mn^{4+} are ordered in the $\left[(Mn^{4+}_{0.68}Mn^{3+}_{0.32})O_2\right]^{0.32-}$ layer. A structural model is proposed, in which Mn^{4+} and Mn^{3+} are ordered similarly to Al and Li in the $\left[(Al^{3+}_{0.67}Li^{+}_{0.32})(OH)_2\right]^{0.32+}$ layer, with Mn^{3+} cations being surrounded by six Mn^{4+}, and Mn^{4+} cations by three Mn^{3+} and three Mn^{4+}. Similar cation ordering in the manganese and aluminium layers likely provides a more homogeneous local balance of the excess and deficit of charges in each layer and increases the stability of lithiophorite. Ni (r = 0.70 Å) substitutes for Mn ($r(Mn^{4+})$ = 0.54 Å, $r(Mn^{3+})$ = 0.65 Å) in the manganese layer in the natural lithiophorite. In contrast, Zn (r = 0.74 Å) fills vacant sites in the gibbsitic layer of natural lithiophorite, in a similar manner as lithium (r = 0.74 Å) in synthetic lithiophorite. The partitioning of Ni and Zn between the two layers is a result of the general preference of Ni, whose size is intermediate between those of Mn^{3+} and Li^{+}, for slightly smaller

sites. In contrast with nickel, which is detected only where there is lithiophorite, the Zn-lithiophorite association found in Fe-Mn mottles is not representative of the bulk soil. The combined use of X-ray diffraction, and powder and polarized EXAFS spectroscopy revealed that Zn is predominantly bound to hydroxy-Al interlayers sandwiched between 2:1 vermiculite layers in the fine soil matrix. The incorporation of Zn in the gibbsitic layer of both lithiophorite and vermiculite helps increase the stability of these minerals by providing positive charge to balance the negative charge from the 2:1 phyllosilicate layer and the $\left[(Mn^{4+}_{0.68}Mn^{3+}_{0.32})O_2\right]^{0.32-}$ layer of lithiophorite. This binding environment for zinc is probably the main mechanism by which zinc is sequestered in acidic to near-neutral aluminium-rich clayey soils.

1. INTRODUCTION

Understanding how trace elements are sequestered at the molecular scale in surface and near-surface continental environments is critical to (1) developing a scientific basis for maintaining soil quality, (2), predicting the evolution of metal speciation in contaminated soils and, (3), formulating effective strategies to clean up severely contaminated areas. The work reported here addresses these issues which have societal importance, and is also part of a larger effort to determine the natural speciation of Ni, Zn, As, and Pb in uncontaminated soils from several continents. In this ongoing program, the chemical forms of Ni and Zn in ferromanganese nodules from a rendzic lithosol (pH < 7, Baize and Chrétien, 1994) developed on Sinemurian limestones (France) and from the fragipan horizon of a loess soil (pH = 4.5 - 5.0) of the Mississippi Basin (USA) have been investigated (Manceau et al., 2002a, 2002b, 2003). We demonstrated that nickel is preferentially contained in the manganese layer of lithiophorite, a mixed MnO_2-$Al(OH)_3$ phyllomanganate commonly found in acidic soils (Chukhrov et al., 1985; Scott, 1987; Taylor et al., 1964). The crystal chemistry of zinc is more variable for at least two reasons. First, zinc has a versatile tetrahedral and octahedral coordination chemistry due to its lack of crystal field stabilization energy in either coordination. Second, the effective ionic radius of zinc differs by less than 10% from those of $^{VI}Al^{3+}$ (0.53 Å) and $^{VI}Fe^{3+}$ (0.64 Å) in four-fold coordination (0.60 Å for $^{IV}Zn^{2+}$), and from those of $^{VI}Mg^{2+}$ (0.72 Å) and $^{VI}Fe^{2+}$ (0.78 Å) in six-fold coordination (0.74 Å for $^{VI}Zn^{2+}$), thus allowing its incorporation in a large number of soil minerals. Among the panoply of Zn-bearing primary and secondary minerals already identified in nature, three are frequently found in acidic surficial environments: ^{IV}Zn-sorbed birnessite, ^{VI}Zn-incorporated lithiophorite and ^{VI}Zn-containing hydroxy-Al phyllosilicate (Isaure et al., 2005; Manceau et al., 2000a; Manceau et al., 2002a; Manceau et al., 2004; Manceau et al., 2003; Nachtegaal et al., 2005; Roberts et al., 2002;

Scheinost et al., 2002) (Fig. 1). At near-neutral to slightly alkaline pH, zinc can be speciated also as phosphate, trioctahedral phyllosilicate, and hydrotalcite (Isaure et al., 2005; Juillot et al., 2003; Nachtegaal et al., 2005; Panfili et al., 2005). ^{IV}Zn-sorbed ferrihydrite and Zn-incorporated goethite also are found commonly, apparently over a large pH range as long as it is not too extreme (Isaure et al., 2002; Manceau et al., 2000a; Manceau et al., 2003; Nachtegaal et al., 2005; Roberts et al., 2002).

The present study extends our previous work on the natural speciation of nickel and zinc in acidic environments by examining the case of the argillic horizon of an Ultisol in Taiwan used for rice crops until 1991. This former cultivated paddy soil is characterized by a high clay content and shrink-swell potential, and is representative of the majority of imperfectly drained agricultural soils developed under warm subtropical temperature regimes. In these soils, seasonal wetting and drying cycles provide the primary control of the dissolution and precipitation of redox-sensitive minerals, especially Fe and Mn (oxyhydr)oxides. Fe and Mn are mobilized by reduction and then concentrated upon oxidation in various forms, among which pore infillings, mottles and concretions are the most frequent. The abundance of Fe and Mn concretions surrounded by areas depleted of Fe increases as cycling of oxidation and reduction conditions increase in rice production (Hseu and Chen, 2001). These soils are also of interest because of their similarity to nodule-containing vertisols that are well preserved in the geologic record including the Carboniferous (Stiles et al., 2001)

In this work, we seek to answer three questions: what are the mineral hosts of nickel and zinc? How are the two trace elements incorporated in the mineral structures? What is their dominant speciation in the bulk soil? Zn and Ni may be contained in any mineral, either as structural impurities incorporated by co-precipitation or as sorbed surface complexes. The structural chemistry of foreign ions can be studied by established X-ray spectroscopic and diffraction methods, but even the most highly developed X-ray analysis tools require some minimum amount of nearly-pure single phases. With a lateral resolution of a few tens of square

micrometers and a typical absorption length of order 30 μm at 10 keV, new hard X-ray microbeam techniques now bring powerful X-ray diffraction and spectroscopy methods, long reserved for large samples, to the grain scale of most environmental materials (Manceau et al., 2002a; Marcus et al., 2004b; Sutton et al., 2002). We have addressed the first two questions using nondestructive, high precision X-ray synchrotron-based microfluorescence (μ-SXRF), microdiffraction (μ-XRD), and micro-extended X-ray absorption fine structure (μ-EXAFS) spectroscopy. The third question is answered by applying powder EXAFS spectroscopy to a sample representative of the soil volume. Since the soil is argillic and we know that zinc has a high affinity for phyllosilicate in nature (Manceau et al., 2000a, 2004; Panfili et al., 2005), the polarization dependence of EXAFS measurements on a uniaxially oriented clay preparation of the soil sample was used with the other techniques to determine precisely the bonding environment of zinc in this pool. Polarized EXAFS (P-EXAFS) measurements in combination with powder X-ray diffraction were instrumental in demonstrating the incorporation of zinc in the hydroxy-Al layer of vermiculite. Since hydroxy-Al phyllosilicate is abundant in Ultisols (Hseu et al., 2004; Li et al., 1998), which cover a large part of the earth's surface, this species is likely one of the most abundant forms of Zn in the environment.

2. MATERIALS AND METHODS

2.1. Materials

2.1.1. Sampling site

The Hsinwu soil has been chosen for this study because it belongs to a toposequence whose pedology, hydrology, and geochemistry have been characterized in great detail by Dr. Z.S.

Chen and coworkers in the past decade, and because the micromorphology of the particular sample studied here is typical from the Btv horizon of Ultisols (Hseu and Chen, 1997; Hseu and Chen, 1999). The Hsinwu soil is located on the upper Chungli Terrace in northern Taiwan, about 40 km southwest of Taipei City (Hseu and Chen, 2001). The Chungli Terrace is made of alluvial material from the Quaternary period, and has a slope between 1 and 7 %, declining gently from the eastern hills to the western seashore. Climatic data show a mean air temperature of 27^{o}C in summer and 13^{o}C in winter. The average annual rainfall over the last decade is 1,560 mm, with a minimum rainfall in winter. The agricultural lands on the Chungli Terrace have been used for rice (*Oryza sativa* L.) production since the 1950s. Each year, rice is harvested twice between March and October, and the soils lie fallow in the winter. Rice production at the Hsinwu site studied here has been stopped since 1991, so the surface soil has never been flooded in the last 14 years.

The hydromorphic and redox regimes of the Hsinwu soil were monitored for two years in 1996-1997 (Hseu and Chen, 2001). Briefly, the soil at depths of 25, 75, 100, and 200 cm was saturated for 40 %, 45 %, 50 %, and 65 % of the time, respectively. Because of the higher elevation of the soil, and hence its good drainage, Eh values at all depths were generally close to 250 mV, indicating oxidizing conditions. Moderately reducing conditions with Eh values ranging from -50 to +50 mV occurred below 75 cm from January to August in 1996 and from May to July in 1997. On average, the soil at 25, 75, 100 and 200 cm below the surface was reduced for 10 %, 25 %, 30 %, and 10 % of the time annually, respectively. The studied sample was collected in the Btv horizon at 120 cm depth. At this depth, the soil is saturated for about 50 % of the year and reduced for 20 % of the year due to the fluctuation of the groundwater table. This cycling produces a fluctuation over time of the Fe^{2+}/Fe^{3+} and Mn^{4+}/Mn^{2+} ratios and, hence, a segregation of Fe and Mn in the soil profile resulting in the formation of millimeter-sized Fe-Mn concretions (Hseu and Chen, 1996; Hseu and Chen, 1997). The Btv horizon contains 30 % of concretions by weight.

2.1.2 Samples

Chemical analyses showed that zinc and nickel are contained in the fine clay fraction of the soil (42 and 46 mg/kg, respectively), in major ferruginous soft mottles (54-57 and 43-50 mg/kg, respectively), and in minor ferromanganiferous mottles (73 and 112 mg/kg, respectively). These three parts of the soil were prepared as follows for metal speciation. One kilogram of soil was homogenized, sieved at < 2 mm, and the <2 μm clay fraction separated by centrifugation at 700 rpm for 8 min. Then, the <0.2 μm fine fraction was extracted by continuously centrifuging the <2 μm fraction at 4000 rpm for 25 min. A self-supporting film was prepared from the <0.2 μm fraction by slowly filtering the suspension through a 0.05 μm Sartorius cellulose nitrate filter. The resulting thin film was cut in 5 x 20 mm^2 pieces and stacked on a sample holder for P-EXAFS and crystallographic texture measurements. A thin film from the <2 μm fraction of the Redhill montmorillonite ([Zn] = 85 mg/kg, Redland Minerals), Surrey, England was prepared in the same way as a reference material. Twenty medium-size mottles were separated by hand from the soil matrix and ground with a mortar and pestle. The powder was dry-sieved and the < 50 μm fraction was pressed into pellets for powder EXAFS measurement. Finally, an Fe-Mn mottle was dried at 80°C overnight in an oven, then impregnated with high purity resin (Scotchcast™ epoxy), and a 30 μm-thick micropolished thin section prepared for μ-SXRF, μ-XRD and μ-EXAFS measurements.

2.2. Methods

2.2.1. Chemical analyses

The soil exclusive of soft mottles, four individual Fe mottles, and one Fe-Mn mottle were analyzed by Inductively Coupled Plasma Atomic Emission Spectrometry (ICP –AES) for Al, Mg, Ca, Fe, Mn, Na, K, P, Ti, Sr, Ba, Ni, Cr, Zn, Cu, V, and Zr concentrations, and by Inductively Coupled Plasma Mass Spectrometry (ICP-MS) Fisons VG-Plasma for Co, Rb, Nb, Mo, and REE concentrations. Each sample was quantitatively digested with ultrapure concentrated HF + HNO_3 + H_3BO_3 acids. After acid digestion, the solution was dried and re-dissolved in 1M HNO_3. About 2/3 of this solution was used for ICP –AES analyses, and 1/3 for ICP-MS. With a detection limit of about 1 to 2 ppb for ICP-AES and about 0.01 ppb for ICP-MS, a minimum amount of 10 ng and 0.1 ng of individual elements in each sample was required for element measurements by ICP-AES and ICP-MS, respectively. For both techniques, the BE-N international basalt was used as standard. The overall analytical uncertainty is about 10 % (2σ) for ICP-AES and 5% (2σ) for ICP-MS analyses.

2.2.2. X-ray diffraction

The clay mineralogy was studied by X-ray diffraction on the <2 mm and <2 μm fractions. The clays (<2 μm fraction) were decarbonated overnight with buffered (pH 5) sodium acetate solution, and Mg-saturated with 0.5 M $MgCl_2$ for glycerol (G) and ethylene glycol (EG) saturation, and K-saturated with 1.0 M KCl for heat treatment at 100, 300, and 550 °C. Suspensions were shaken in the saline solutions for 12 hours minimum, and the exchange was repeated three times for complete exchange of interlayer cations. Excess chloride was rinsed out by centrifugation in water. Oriented aggregates of Mg- and K-saturated clays were prepared by air-drying 30 mg of material from aqueous suspension onto glass slides. Glycerol solvation was performed by pressing the oriented slides on glycerol-soaked filter paper. Excess liquid glycerol

was removed by pressing the wet slide onto dry paper. Ethylene glycol saturation was performed by leaving an oriented mount on the shelf of an EG-containing desiccator placed overnight in an oven at 60°C. XRD patterns were recorded with a Bruker D5000 diffractometer equipped with a Cu anode and a Si(Li) solid state detector. All patterns were recorded at a 0.02° 2θ step interval and with a 12 s count time.

2.2.3. Quantitative texture analysis

The orientation distribution of mica, interstratified illite/mica - vermiculite, lepidocrocite and kaolinite in the soil thin-film and of Redhill montmorillonite were determined by texture analysis in order to verify that the degree of orientation of the clay platelets was high enough for quantitative P-EXAFS analysis. Measurements were performed in reflection mode using a four-circle diffractometer equipped with a CPS 120 (INEL) position sensitive detector that spans all the necessary 2θ range at once (Lutterotti et al. 2004). The incident X-ray beam was monochromatized with a flat graphite slab of 0.4° mosaic spread set up for Cu Kα radiation selection, and collimated to 1 mm x 1 mm point focus to ensure full interception of the beam by the sample at any angle. The self-supporting films were mounted on a <001>-oriented silicon single crystal slide to minimize the background contribution from the sample holder. Since for self-supporting films of clay minerals, single fiber textures are observed with the <001>* fiber direction being parallel to the film normal, then only tilt ρ-scan measurements are necessary (Manceau et al., 1998). The distributions of the 002-mica (2θ = 17.7º), 002-illite/mica - vermiculite ($2\theta \sim 18.4$º), 020-lepidocrocite (2θ = 14.0º) and 001-kaolinite (2θ = 11.5º) Bragg reflections against the tilt ρ angle were measured in the soil sample with the film plane perpendicular to the fiber axis at $\rho = 0°$ (a specimen mounted for conventional Bragg diffraction has $\rho = 0°$). The 002-mica reflection is partially overlapped with the 002 line from

the interstratified illite/mica - vermiculite component, and the assemblage was decomposed in the 2θ space for each ρ orientation using pseudo-Voigt peak shapes. Although lepidocrocite is a minor phase in the bulk sample, its 020 reflection was apparent on the pattern for the film from the <0.2 μm soil fraction and, thus, its orientation distribution was calculated as well. The full width at half maximum of the orientation distribution (FWHD) of the 00ℓ (phyllosilicate) and 020 (lepidocrocite) lines were calculated using the formalism described by Guilmeau et al. (2004). The distribution densities are expressed in multiples of a random distribution (m.r.d. units) and take a constant value of 1 m.r.d. over all ρ angles for perfectly randomly oriented powders, whereas <001>* fiber textured samples exhibit a maximum density for $\rho = 0$, and a progressively lower density value at increasing ρ angles. The higher the texture strength, the narrower is the distribution in density. For phyllosilicates, Manceau and Schlegel (2001) showed that P-EXAFS spectra have a single crystal-like angular dependence when the FWHD is lower than 30-40°, in which case no texture correction needs to be introduced in the quantitative analysis of EXAFS data. For FWHDs larger than ~60-70°, textural effects on P-EXAFS data steadily vanish due to the progressively isotropic character of the film.

2.2.4. Mn, Ni and Zn micro-spectroscopy and micro-diffraction

X-ray microscopic measurements were performed at the Advanced Light Source (Berkeley) on 10.3.2 (μ-SXRF and μ-EXAFS) and 7.3.3 (μ-XRD) stations using a set-up similar to that used in previous studies (Manceau et al., 2002a; Manceau et al., 2002b; Marcus et al., 2004a). The distributions of Mn, Fe, Ni and Zn in the ferromanganiferous mottle were imaged by scanning the thin section in the focused beam at 10 keV. A large overview map from a 3800 x 2800 μm area was measured first at 15 x 15 μm resolution, then two detailed maps of 2100 x 1800 μm and 1400 x 650 μm each were recorded at 9 x 9 μm and 7 x 7 μm resolution,

respectively. The count time was set at 200 milliseconds, and the beam dimension was adjusted to be slightly smaller than the step size. The characteristic Kα fluorescence line intensities of the elements were measured with a seven-element Ge solid-state detector, and normalized to the intensity of the incoming monochromatic beam. No attempt was made to calculate elemental concentrations because of the difficulties inherent to this quantification (Sutton et al., 2002), and the focus on relative element distributions rather than concentration. Micro-XRD patterns and Mn-, Ni-, and Zn-K edge μ-EXAFS spectra were collected on selected representative regions in the thin section, based on elemental associations obtained from μ-SXRF mapping. The various points-of-interest (POIs) were relocated from one beamline to another using μ-SXRF. Point μ-XRD patterns were collected in reflection geometry with a photon energy of 6 keV, a beam size on the sample of 15 μm x 20 μm in the horizontal and vertical directions, respectively, and a 1024 x 1024 pixels Bruker CCD camera, with an exposure time of 120 s. Multiple EXAFS spectra were collected in fluorescence-yield detection mode using the same seven-element Ge detector as for μ-SXRF. The total counting time was 54 s/point for the Mn spots and 240 s/point for the Ni and Zn spots, and the integrated number of fluorescence counts was 10 x 10^6 for Kα Mn, 3.6 x 10^6 for Kα Ni, and 1.3 10^6 for Kα Zn.

2.2.5. Zn powder and polarized EXAFS spectroscopy

Powder and polarized Zn K-edge EXAFS spectra were collected in fluorescence-yield detection mode using a 30-element Ge solid-state detector on the FAME spectrometer at the European Synchrotron Radiation Facility (ESRF, BM30B). P-EXAFS measurements were carried out at incident angles between the electric field vector and the film plane of $\alpha = 10°$, 35°, 55° and 80° (Manceau et al., 1998). Powder EXAFS measurement on the homogenized powder was performed at the magic angle ($\alpha = 35°$, Manceau et al., 1988).

All EXAFS data were treated using home-made software for data normalization and Fourier transformation, and WinXAS (Ressler, 1998) for spectral simulations. Fourier transformations were done on the entire $k^3\chi(k)$ curves shown in the Results section under a Kaiser-Bessel window ($\tau = 3$). Transformation from reciprocal (k) to real (R) space produces radial structure functions (RSFs) with peaks corresponding to average absorber-backscatterer distances, but deviating from the true distance ($R + \Delta R$) due to a phase shift. Spectral simulations were performed on Fourier filtered data using Zn-O, Zn-Al and Zn-Si phase shift and amplitude functions calculated with FEFF 8.20 (Zabinsky et al., 1995) from a Zn-substituted montmorillonite cluster (Richardson and Richardson, 1982). Fits were performed with the minimum number of atomic pairs and adjustable parameters necessary to reproduce the data. In particular, ΔE, the difference between the observed and fitted energies of the edge jump, was treated as a single adjustable parameter for all sets of backscattering atoms, and for polarized data R and σ parameters for the Al and Si shells were constrained to their values at $\alpha = 35°$ and 80°, respectively. Depending on sample spectra, the number of independent points (N_{ind}) as calculated by the Nyquist formula $N_{ind} = (2\Delta R\Delta k)/\pi$ (ΔR is the width of the R-space filter window, and Δk is the fit interval in the k space), outnumbered the number of free parameters by at least 3, and up to 7. Typical errors are ± 0.02 Å for the interatomic distances (R), and ± 20 % for the coordination numbers (CN). The amplitude reduction parameter, S_0^2, was fixed at 0.8.

3. RESULTS AND INTERPRETATIONS

3.1. Chemical compositions

Elemental concentrations in the four Fe-enriched mottles (FeMots) and the ferromanganiferous mottle (FeMnMot), and the enrichment factor (EF) for each element relative to the soil matrix, are given in Figure 2. A selection of individual analyses is reported also in Table 1. The mottles have Fe concentrations in the range 3.7 – 7.1 wt. %, and the ferromanganiferous mottle a Mn concentration of 4.4 wt. % and a Mn/Fe ratio of 1.1. On average, Fe is enriched 8 times in FeMots and 6 times in FeMnMot relatively to the soil matrix, and Mn is enriched 2 and 233 times, respectively. Consistent with the difference of chemical composition between the two types of mottles, the purely ferruginous mottles were extremely crumbly and the ferromanganiferous ones moderately hardened. Generally speaking, the higher the amount of Fe and Mn, the harder are the soil nodules as these concretions consist of soil material cemented by Fe and Mn oxides.

The FeMots samples have essentially the same trace metal composition as the soil matrix, except for Pb and P, whose EFs are 3.3 and 2.7, respectively. The observed enrichment in P is in accordance with the tight association of phosphate with Fe oxides in fertilized soils (Ruiz et al., 1997), and with the chemistry of P in aquatic systems, which is often controlled through interaction with Fe (Syers et al., 1973). Koschinsky and Hein (2003) also showed that Fe oxides are more efficient at sequestering oxyanions than Mn-oxides in marine ferro-manganese concretions. Similarly to P, the partitioning of Pb in the Fe mottles is consistent with the known affinity of Pb for Fe oxides (Kabata-Pendias, 1980; Koschinsky and Hein, 2003; Latrille et al., 2001; Ostergren et al., 1999). For example, Li (1982) and Palumbo et al. (2001) showed that Pb correlates with Fe in marine and soil Fe-Mn nodules. However, the Pb partitioning is four times higher in FeMnMot than in FeMots, suggesting that Pb is preferentially bound to Mn oxides over Fe oxides. This result is in agreement with flow-though Pb sorption experiments, which showed that Mn oxides, and in particular birnessite, have a higher efficiency for Pb sorption than Fe oxides (O'reilly and Hochella, 2003). The higher sorption efficiency of birnessite is due, firstly, to the hydration and size of its interlayer space (~ 5.3 Å in the one-layer hydrated form

and ~ 8 Å in the two-layer hydrated form), which is large enough to accommodate big cations such as Pb^{2+} ($r(^{VI}Pb^{2+})$ = 1.18 Å) and, secondly, to the high surface charge resulting from structural defects (Mn^{3+} for Mn^{4+} substitution, vacant Mn layer sites) (Drits et al., 2002; Lanson et al., 2002b). For example, the charge density is as high as -0.3 unit charge per octahedron in triclinic birnessite, that is about three times higher than that in montmorillonite. Note, however, that the EF may vary with the mineralogy of Mn oxides in Fe-Mn nodules because not all phyllomanganates have a high efficiency for Pb sorption. Lithiophorite, which is abundant in the studied soil and has a similar charge as triclinc birnessite (+0.32 per octahedron), has a low Pb sorption efficiency because its interlayer space is dehydrated and does not swell. Other factors may account as well for the variability of the Pb EF in nodules, such as the temporal variation in composition of pore solutions. Finally, the expected dominant aqueous species of Pb, Pb^{2+}, in the soil solution (oxidizing conditions and pH ~ 5.5, Hseu and Chen, 2001) also accounts for the higher affinity of this element for Mn oxides, because Pb complexation with carbonates ions (expected in freshwater at pH > 7) would have led to a more exclusive association with Fe oxides (Koschinsky and Hein, 2003; Palumbo et al., 2001).

The oxidation of soluble Co(II) and Ce(III) to insoluble Co(III) and Ce(IV) by Mn oxides accounts for the enrichment of these two elements in FeMnMot (49 and 2.3, respectively) (Bidoglio et al., 1992; Manceau et al., 1997; Ohta and Kawabe, 2001; Takahashi et al., 2000; Vaniman et al., 2002). Cerium is known to behave differently from other rare earth elements (REEs), which are exclusively trivalent (except for Eu(II)/Eu(III)) and whose EF values do not differ significantly from 1 (except possibly for La). Our measured Ce anomaly is consistent, though generally lower, with data reported in the literature on the partitioning of this element in Mn-rich samples (e.g., De Carlo and Mcmurtry, 1992; Fukuda et al., 1998; Palumbo et al., 2001; Takahashi et al., 2000). The relatively low EF value for Ce may partly result from the somewhat low abundance of Mn in FeMnMot, rather than an unusually low Ce content since its concentration in FeMots (46 ppm on average) and in the soil matrix (67 ppm) are similar to

shale values (60-70 ppm, Gromet et al., 1984). This relatively low EF may be linked also to the low pH (~5.5) of the Lungchung soil. Indeed, Ohta and Kawabe (2001) showed that the partition coefficient of Ce on Mn-oxides decreases by a factor ~30 when the pH decreases from 7 to 5.5.

FeMnMot is also enriched in Ba (EF = 3.0), Mo (EF = 2.5), Ni (EF = 2.4), and to a lesser extent Zn (EF = 1.7), as usually observed in continental and oceanic Mn nodules and crusts, and Mn permeated clay bodies (e.g., Childs, 1975; Dawson et al., 1985; Kasten et al., 1998; Koschinsky and Hein, 2003; Palumbo et al., 2001; Uzochukwu and Dixon, 1986; Vaniman et al., 2002). Manceau et al. (2003) explained the higher Ni over Zn EF value in soil nodules by the higher affinity of Ni for lithiophorite and the lack of marked Zn selectivity for one specific soil mineral. In soil, Zn is generally bound to both Mn oxides and phyllosilicates, and occasionally to Fe oxides. Since layer silicates are distributed almost evenly inside and outside ferromanganese nodules, the Zn distribution is more homogeneous than that of Ni and, consequently, Zn has a lower EF value.

3.2. XRD

Bulk soil mineralogy includes quartz, muscovite, chlorite, microcline, albite, and minor anatase and poorly-crystalline goethite. Quartz and phyllosilicates prevail, with the layer silicates giving intense reflections at ~10 Å (001), 4.45-4.46 Å (02-11), 2.56 Å (13-20), and 1.49-1.50 Å (060). The mineralogy of the <2 μm size fraction is composed dominantly of illite/mica (*d*-spacings of 10.0, 5.00, and 3.34 Å), and ordered and disordered kaolinite (*d*-spacings of 7.14 and 3.57 Å), with lesser amounts of vermiculite (*d*-spacing of ~14.3 Å), mixed-layer illite/mica – vermiculite (*d*-spacings of ~24, ~12, and ~4.7 Å), chlorite (*d*-spacing of 14,1, 4.7, 3.5 Å), goethite, microcline, albite and quartz (Fig. 3a). Upon glycerol and ethylene glycol solvation, the peak at 14.4 Å vanished and no particle expanded to higher d

values. This behavior identified vermiculite and excluded smectite, which expands with both G and EG (Douglas, 1989; Malla and Douglas, 1987; Moore and Reynolds, 1997). The vermiculite particles did not collapse spontaneously to 10.2 Å after K-saturation and gentle heating (Fig. 3b). They remained expanded to temperatures greater than 100 °C, and collapsed only partly at 550 °C, as attested by the strongly asymmetrical shape of the basal reflection at 10.1 Å. This thermal behavior is characteristic of hydroxy-Al interlayers (Douglas, 1989), which compensate partially the charge deficit of the vermiculite layers. Hydroxy-Al complexes that are not developed into complete interlayer sheets are common in aluminum-rich acidic clayey soils with restricted drainage (Chen et al., 2001; Manceau et al., 2004; Marques et al., 2002). This clay species is relatively abundant in this paddy soil, as shown by the height of the ~14.3 Å reflection at room temperature, and the intensity of the scattering hump at 10.5 – 12 Å at 550 °C.

3.3. Texture goniometry

Since the X-ray diagrams for the two film samples were recorded at fixed incidence angle, peak intensities differ from those presented before and measured with a classical θ-2θ Bragg-Brentano setup (Fig. 4). For example, the magnification of the 002 reflection of mica at 2θ = 17.7° in the soil film sample is due to the fact that its pattern was recorded at ρ = 0° and an incidence angle of 8°. Similarly, the XRD pattern of the Redhill montmorillonite was recorded at ρ = 0° and θ = 3°, thus enhancing its 001 reflection at 5.8° 2θ. Due to the high orientation of the basal planes of platelets in the film plane, no *hkl* reflections were observed. The film texture can be visualized also on pseudo 3D diagrams by plotting the peak intensity against ρ. An example is presented in Figure 5, which shows the complete disappearance of the 002-mica peak at ρ angle as low as 15°, thus confirming the strong texture of this phase.

Although the one-dimensional and pseudo 3D diagrams can be used to reveal the successful achievement of a texture, they do not provide quantitative information on its strength. This information was obtained by integrating and normalizing the 2θ positions against ρ angles, which yielded the angular distribution density profiles presented in Figure 6. Both lepidocrocite and mica exhibit extremely high texture strengths with FWHDs values of about 12° and density levels as high as ~150 m.r.d.. These values represent the largest textures ever reported in the literature for a self-supporting clay film. So far, the highest degree of alignment of clay platelets in a film was obtained for Garfield nontronite with a FWHD of 20° and a density of 40 m.r.d. (Manceau et al., 1998). The lepidocrocite and the mica textures are similar and could be fit satisfactorily assuming a Gaussian mosaic spread (Jeffery, 1923). The textural similarity of the two minerals, despite their different chemical composition and crystal structure, is probably not fortuitous, and may be due to epitaxy between the lepidocrocite (010) planes and the (001) mica planes, similar to the epitaxy of goethite and hematite on kaolinite described in a soil from Cameroon (Boudeulle and Muller, 1988). The illite/mica - vermiculite and the kaolinite phases have larger distributions with FWHDs of 30° and 36.5°, respectively. The kaolinite peak is broadened on its left tail, suggesting that the sample comprises several populations of kaolinite particles having different sizes. During the filtration process used to elaborate the films, small particles tend to deposit later and to fill in the pore spaces left between the already settled largest crystallites, thereby disrupting the alignment of the finest particles. Therefore, the difference of texture strength between mica and lepidocrocite, on one hand, and illite/mica - vermiculite and kaolinite, on the other hand, may arise from a difference in crystallite size. All in all, the four mineral species had a high degree of orientation in the film plane, and the Zn P-EXAFS spectrum of the soil film sample was expected to exhibit a strong angular anisotropy regardless of the host Zn phase since the diffraction intensities rapidly fell off above the magic angle of 35° (i.e., all densities rapidly reached 0 m.r.d.). This finding also stands for the Redhill montmorillonite, whose FWHD equals 25.5° (Fig. 6e). The texture strength of the two films is

high enough to allow the probing of the three-dimensional local structure of Zn by P-EXAFS without loss of angular resolution as compared to single crystals.

3.4. Speciation of Mn, Ni and Zn in a Fe-Mn mottle

3.4.1 μ-SXRF

The entire area of a thin section of an Fe-Mn mottle one cm in diameter was examined by μ-SXRF, and the mineralogy and crystal chemistry of Ni and Zn is completely represented by the region presented in Figure 7a. This large overview map shows irregular Fe-Mn impregnations of the groundmass. Similar pedogenic textures were observed in the fragipan (Btx) horizon at ~80-130 cm depth from a hydrosequence of a high terrace of the Ohio River (USA) (Manceau et al., 2004). Segregation of Fe and Mn in soft masses, and their depletion in the surrounding soil matrix, are typical redoximorphic phenomena observed in all Btv horizons with clay textures, and results from the alternating oxidation and reduction cycling caused by the fluctuation of groundwater (Vepraskas and Wilding, 1983; Southard and Buol, 1988; Stolt et al., 1994). Numerous root channels partly infilled with Fe and Mn (oxyhydr)oxides and phyllosilicates (see next section), and imaged in green (Fe) and blue (Mn) on the two-color GB (Green-Blue) maps, are indicative of downward transport (eluviation) and accumulative deposition where flow is restricted (illuviation). Illuvial accumulations of fine particles along roots are commonly observed in rice-growing Ultisols (Hseu and Chen, 2001; Hseu and Chen, 1996; Hseu and Chen, 1997), and more generally in accumulative horizons (Vaniman et al., 2002). Another chemical signature of the migration of Fe is the downward flame-like Fe differentiation shown in Figure 7b, which ends with a peninsula shaped ferrugineous texture suggestive of a top-down permeation of the clay matrix by Fe (oxyhydr)oxides. Fine mapping of two areas from the coarse map clearly shows that Mn oxides do not occur only as pore

coatings, but have also permeated the groundmass as indicated by the presence of diffuse blue patches within the clayey matrix (Fig. 7b,c). The petrographic and chemical observations all confirm connection of this horizon to the surface, principally through the evidence of root penetration and of Fe and Mn eluviation textures.

When Zn and Ni are added in red to the previous maps in proportion to the fluorescence signal, some of the blue areas turn violet (blue + red), but none of the green areas turn yellow (green + red), indicating that the trace metals are co-associated spatially to Mn oxides. This Zn/Ni-Mn association and the lack of Zn/Ni-Fe correlation detected at the micrometer-scale are consistent with the chemical analyses of the individual mottles, which showed that the ferro-manganiferous mottle was enriched in Ni and Zn, but not the ferriferous. An average X-ray fluorescence spectrum from the extended area was obtained by recording continuously the fluorescence signal while scanning the sample under the excitation beam (Fig. 8a). Mn/Fe, Ni/Fe, and Zn/Fe atomic ratios were estimated from the relative intensities of the Mn, Fe, Ni and Zn Kα fluorescence lines after correction of matrix absorption effects and fluorescence yields. The studied area has about 1.3 times less Mn, 300 times less Ni, and 250 times less Zn than Fe, in qualitative agreement with the wet chemistry analyses of the individual mottle (Table 1). The prevalence of Zn over Ni is indicated in the RGB (Red-Green-Blue) maps by the fact that all the Ni-Mn pockets also contain Zn, while a number of Zn-Mn areas lack Ni. Spots which contain both Zn and Ni have a variable Ni/Zn ratio, since some of them are brighter when the red channel codes for Ni, whereas other spots become brighter when red codes for Zn. This is clearly apparent in Fig. 7c, which shows three aligned Mn pockets to the left of the root channel that turned bright red upon adding nickel (I(Ni-Kα) ≈ 2800 counts/s) and dim violet upon adding Zn (I(Zn-Kα) ≈ 1100 counts/s). Alternately, a hot spot marked by an arrow to the lower right of the root channel has major Zn (I(Zn-Kα) = 2300 counts/s) and minor Ni (I(Ni-Kα) = 600 counts/s), and the Zn diffuse area to the right of the root channel is also rich in Zn,

but relatively poor in Ni. Some Mn areas, in particular that contained in the lacy Fe area of the upper left part from the coarse map (Fig. 7a), lack Zn and Ni. The uneven distribution of Zn relative to Ni, and the uneven distribution of these two elements relative to Mn may originate from a time fluctuation of the chemical composition of the soil solution, or may be controlled by the soil mineralogy since Mn oxides include a large number of species with contrasting affinity for trace metals (O'reilly and Hochella, 2003). In the following, μ-XRD will be used to determine whether the three chemically distinct Mn populations (Zn- and Ni-free, Zn- and Ni-containing, and Zn-containing but Ni-free) also differ in mineralogy.

3.4.2 μ-XRD

Two-dimensional diffraction patterns were recorded at one dozen of POIs together with the X-ray microfluorescence spectra (Fig. 8 and 9). Lithiophorite was always detected wherever there was Mn and Zn, independently of the presence of nickel. In particular, POI-1 and POI-2 exhibited similar diffraction patterns despite their difference in trace metal content. Therefore, the variation in Ni/Zn ratio observed by μ-SXRF does not seem to correspond to a variation in mineralogy, and supposedly reflects a spatial and temporal variation in the composition or in the physico-chemical properties of pore water. Manganese was mineralized as turbostratic hexagonal birnessite (i.e., vernadite or natural δ-MnO_2) where there are no trace metals (e.g., POI-3 and POI-4; Fig. 8c,d). This species was identified by its diffraction maxima at 7.1-7.2, 2.4 and 1.42 Å (Drits et al., 1997), and the disappearance (1.42, 7.1-7.2 Å) or weakening (2.4 Å) of these broad peaks when point XRD patterns were collected a few tens of microns away from local Mn maxima. Birnessite and lithiophorite are the most common Mn minerals in soils (Chukhrov and Gorshkov, 1981; Mckenzie, 1972; Taylor, 1968; Taylor and Mckenzie, 1966; Vodyanitskii et al., 2002), and recent studies have shown that nickel selectively occupies the

manganese layer of lithiophorite, probably because of the abundance of Mn^{3+} in this phyllomanganate layer and the similar size of Mn^{3+} (r = 0.65 Å) and Ni^{2+} (r = 0.70 Å). In contrast to Ni, Zn (r = 0.74 Å) can be taken up by lithiophorite and birnessite in soils (Isaure et al., 2005; Manceau et al., 2004; Manceau et al., 2003; Nachtegaal et al., 2005). Here, Zn was never found with birnessite. Point XRD patterns taken in the green areas of the chemical maps (e.g., POI-5) identified goethite as a major mineral species (Fig. 9). Minor hematite was detected at POI-5 in association with goethite (peak at 2.70 Å). Goethite is minor or absent in the Fe-Mn mixed areas from the groundmass (e.g., POI-3 and POI-4), although point SXRF analyses indicated that the two elements are present in similar amounts (Fig. 8c,d). In these areas, the fine matrix is cemented by turbostratic birnessite and poorly crystalline ferric (oxyhydr)oxides (FeOx) which give rise to broad scattering bands at ~2.2 Å and ~1.7 Å in the XRD patterns. This Fe-Mn oxide association, generally referred to as Fe-rich vernadite (Fe-vernadite) and Mn-bearing feroxyhite (Mn-feroxyhite) (Manceau and Combes, 1988; Manceau et al., 1992; Ostwald, 1984a; Varentsov et al., 1991), is common in soils, such as those from the Moscow plain (Vodyanitskii et al., 2002). Minor lepidocrocite and goethite were also identified in the clayey matrix, consistent with the XRD texture analysis.

All the previous minerals are characterized by continuous, homogeneous, and often broad, diffraction rings on the two-dimensional XRD patterns, which are indicative of small, typically nanometer-sized, crystals. In addition to the broad and continuous Debye rings from these essentially nanometer-sized particles, thin homogeneous to discontinuous spotty rings to even single spot reflections from small crystallites and coarse grains were observed on the two-dimensional patterns. The identified minerals include quartz, feldspar (essentially albite), anatase, and 2M muscovite. The phyllosilicate rings were often spotty due to the mixing of large-grained micaceous particles with fine-grained smectite. These well-crystalline species were also identified in the laboratory by powder diffraction.

3.4.3 Mn K-edge μ-EXAFS

The co-existence of two phyllomanganate species in the Fe-Mn mottle found by μ-XRD was confirmed by Mn K-edge μ-EXAFS spectroscopy. The two spectra collected at POI-1 and POI-3 (spectrum Mn-1 and Mn-3, respectively) look different, especially in the 7.5 – 9.5 $Å^{-1}$ interval; the two resonances observed in this spectral region are shifted to lower *k* values for Mn-1 (7.9 and 9.0 $Å^{-1}$) relative to Mn-3 (~8.1 and 9.2 $Å^{-1}$) (Fig. 10a). Recent studies of a large series of phyllomanganate species showed that this region is sensitive to the amount and ordering of Mn^{3+} in the manganese layer (Gaillot et al., 2003; Manceau et al., 2004; Marcus et al., 2004b). When the amount of Mn^{3+} in the layer is nil or low, as in the synthetic turbostratic birnessite, δ-$H_{4y}Na_{4x}(Mn^{4+}_{1-x-y}\square_{x+y})O_2 \cdot zH_2O$ (dBi-1, Villalobos et al., 2003; coded as dBi in Marcus et al., 2004b), the two resonances peak at 8.05 and 9.2 $Å^{-1}$ (Fig. 10b). When the amount of layer Mn^{3+} is high, the two resonances either shift to 7.9 and 9.0 $Å^{-1}$, as in lithiophorite (Mn^{3+}/Mn^{4+} = 0.47; (Yang and Wang, 2003), or the first resonance splits into two maxima at 7.8 and 8.1 $Å^{-1}$ and the second shifts to 8.9 $Å^{-1}$, as in triclinic birnessite (TcBi, $Na_{0.31}(Mn^{4+}_{0.69}Mn^{3+}_{0.31})O_2 \cdot 0.40H_2O$; Silvester et al., 1997) (Fig. 10e). In both cases, the shift to lower *k* values can be explained with reference to the fact that the Mn^{3+} ion is bigger than the Mn^{4+} ion, thus the average Mn-O and Mn-Mn distances, and hence the lattice parameters, are larger in the presence of layer Mn^{3+}. Comparison of the soil spectra with a large series of phyllomanganate references having different, but well-known, Mn^{3+}/Mn^{4+} ratios led us to conclude that the soil lithiophorite (Mn-1) has the same cationic composition as synthetic lithiophorite (32 % Mn^{3+}; Yang and Wang, 2003), and that the stoichiometry of the soil birnessite (Mn-3) is similar to synthetic dBi having 21 % Mn^{3+} (dBi-2, Fig. 10c-d).

Although about one third of manganese is trivalent in TcBi and lithiophorite, the resonance at ~8 $Å^{-1}$ is split in the former but not in the latter manganate. In TcBi, Mn^{3+} cations are ordered

in rows along the [010] direction that are separated by two Mn^{4+} rows along the [100]* direction in hexagonal layer setting (Drits et al., 1997) (Fig. 11a). Owing to the segregation of Mn atoms and the Jahn-Teller distortion of the Mn^{3+} octahedra, the nearest Mn shell (Mn1) is split into two subshells of 2 Mn at ~2.85 Å and 4 Mn at ~2.95 Å, and the third Mn shell (Mn3) is split as well with 2 Mn at ~2.85 x 2 ≈ 5.70 Å and 4 Mn at ~2.95 x 2 ≈ 5.90 Å (Lanson et al., 2002a) (Fig. 11b). The splitting of the Mn3 shell is responsible for the node pattern at $\pi/[2x(5.9\text{-}5.7)] \sim 7.9$ $Å^{-1}$ but not for its 'dunce's cap' shape. Data analysis showed that the node is blunted when the intense Mn5 shell contribution at about ~2.90 x 3 ≈ 8.7 Å is suppressed from the EXAFS spectrum of TcBi because the electronic wave for this shell has a maximum amplitude at 7.8 and 8.1 $Å^{-1}$ and a minimum (i.e., the amplitude is negative) at 7.95 $Å^{-1}$. These structural and spectral considerations lead to the question of whether Mn^{3+} and Mn^{4+} are ordered in lithiophorite as well, and if so, whether this ordering can be detected by EXAFS. To answer this question, a pure and well crystalline sample of lithiophorite was synthesized following the protocol described by Yang and Wang (2003), and a high quality EXAFS spectrum was recorded up to $k_{Max} = 15.5$ $Å^{-1}$. Data are compared to those of dBi-1 (no Mn^{3+}) and TcBi (31% Mn^{3+}) in Figures 12 and 13.

The quantitative spectral analysis was performed using theoretical (Mn-O1, Mn-Mn1) and experimental (Mn-Mn3) amplitude and phase shift functions. The theoretical functions were calculated using the FEFF 7.02 code (Zabinsky et al., 1995) with structure data for lithiophorite, and the experimental functions were derived from dBi-1 taking 6 Mn3 atoms at 5.76 Å. The experimental standards at this distance are from single scattering and three- and four-leg (Mn-Mn1-Mn3) multiple-scattering paths, all with an effective radius of 5.76 Å. The use of these effective functions simplifies the data analysis since it allows one to overlook the contribution from each specific path, thus reducing the number of fitting parameters without degrading the precision of the data. The average EXAFS distance for the first shell of lithiophorite is 1.92 Å, which is shorter than the crystallographic distance by 0.025 Å (Post and Appleman, 1994). The

Mn1 shell of lithiophorite can also be described with a single distance structural model, consisting of 6 Mn at 2.91 Å, in good agreement with the crystallographic value (2.925 Å). The Mn-O and Mn-Mn1 distances of lithiophorite are both larger than those of pure Mn^{4+} manganates (e.g., d(Mn-O) = 1.90 Å and d(Mn-Mn1) = 2.87 Å in dBi-1) because of the bigger size of the Mn^{3+} cation (0.645 vs. 0.53 Å). The increase in interatomic distances in lithiophorite relative to dBi-1 is seen on the overlay plots of the direct ($k \rightarrow R$) and inverse ($R \rightarrow k$) Fourier transforms shown in Fig. 12a and 13a. The $\chi_{Mn\text{-}Mn1}$ electronic waves of the two manganates have a single frequency indicating that the Mn-Mn1 distances are all equal or moderately distributed. However, the lithiophorite wave has a higher frequency due to the larger Mn-Mn1 average distance (Fig. 13a). In contrast, the split of the Mn1 shell in TcBi causes a beat node of the $\chi_{Mn\text{-}Mn1}$ electronic wave at about 13 $Å^{-1}$ (Fig. 13b), and also accounts for the asymmetrical shape of the second FT peak for this reference (Fig. 12b).

In contrast to the Mn1 shell, the Mn3 shell of lithiophorite differs from that of dBi-1 and resembles that of TcBi, in the sense that lithiophorite and TcBi have their fourth (Mn3 shell) FT peak split (TcBi) or broadened (lithiophorite) (Fig. 12b), and their $\chi_{Mn\text{-}Mn3}$ waves exhibit a beat node pattern at ~11.5 $Å^{-1}$ and ~7.0 $Å^{-1}$, respectively (Fig. 13c,d). This contrasts with dBi-1 whose $\chi_{Mn\text{-}Mn1}$ and $\chi_{Mn\text{-}Mn3}$ waves are both monotonous in frequency (Fig. 13a,c). Accordingly, a two-shell model was necessary to fit the lithiophorite and TcBi $\chi_{Mn\text{-}Mn3}$ functions, and the assumption of 4.1 Mn at 5.78 Å ($\Delta\sigma$ = 0.026 Å) and 5.8 Mn at 5.92 Å ($\Delta\sigma$ = 0.026 Å, ΔE = -0.2 eV) for lithiophorite, and 4.5 Mn at 5.79 Å ($\Delta\sigma$ = 0.04 Å) and 5.6 Mn at 6.00 Å ($\Delta\sigma$ = 0.04 Å, ΔE = -2.0 eV) for TcBi, yielded optimal fits between theory and data (Fig. 13e,f).

As noted previously, the split of the Mn3 shell in TcBi (ΔR = 0.20-0.21 Å) is responsible for the wave beating of its EXAFS spectrum at 7.5 – 8.5 $Å^{-1}$ (Fig. 10e). Since the split is decreased to ΔR = 5.92 - 5.78 = 0.14 Å in lithiophorite, the wave beating ought to shift to $k = \pi/[2x0.14] \sim 11.2$ $Å^{-1}$. This inference is supported experimentally by comparing the

lithiophorite EXAFS spectrum to that of dBi-1, in which no structural distortion occurs (Fig. 10e). Another consequence of the reduced distortion of the Mn shell in lithiophorite is the symmetrical shape of its second FT peak, which in this respect looks like dBi-1 (Fig. 12a), and differs from TcBi (Fig. 12b). However, for structural reasons the Mn-Mn1 distances have to be incoherent in lithiophorite as in TcBi since the Mn-Mn3 distances are incoherent in the two species, and the Mn, Mn1 and Mn3 atoms are aligned in the layer plane. In fact, the distance separation between the two populations of Mn1 atoms is only 0.14/2 = 0.07 Å in lithiophorite compared to 0.10 Å in TcBi, and is too small to be resolved by EXAFS spectroscopy. We conclude that the soil birnessite contains about 20 % trivalent manganese, and the soil lithiophorite about 33 % as in its laboratory-derived surrogate. In this latter species, Mn^{3+} and Mn^{4+} cations are not distributed at random otherwise the Mn3 shell would not be split. A structural model for the cation ordering in the MnO_2 layer of lithiophorite is presented in the discussion section.

3.4.4 Ni K-edge μ-EXAFS

A Ni K-edge μ-EXAFS spectrum was recorded up to 11 $Å^{-1}$ at POI-1 (spectrum Ni-1, Fig. 14). The data are identical to those described previously in soil Fe-Mn nodules, in which nickel was shown to substitute for manganese in the MnO_2 layer of lithiophorite (Manceau et al., 2002b). We know from this previous work that the shape of the two first oscillations depends on the Ni site occupancy in lithiophorite. When Ni is incorporated in the MnO_2 layer, the first EXAFS oscillation is asymmetrical on its left side and the second split. Conversely, the first oscillation is split and the second is not when Ni is within the $Al(OH)_3$ layer. This spectral signature was used to determine whether the speciation of Ni was unique in our sample. For this attempt, a dozen micro-extended X-ray absorption near edge structure (μ-XANES) spectra were

collected at different places that differed in Ni/Mn ratios on the sample thin section. No significant difference was found between the μ-XANES spectra; they were all similar to the spectrum recorded at POI-1. We conclude that Ni occurs as only one species. This information could not be obtained by comparing the μ-EXAFS spectrum at POI-1 and the powder Ni-EXAFS spectrum recorded on a representative soil sample because the Ni concentration in the soil is as low as 46 mg/kg, and that the 30-element Ge detector was saturated by the overwhelming parasitic Kα and Kβ signal coming from Fe whose concentration is more than two orders of magnitude higher than Ni ([Fe] = 6.8 g/kg).

3.4.5 Zn K-edge μ-EXAFS

As for Ni, a full Zn K-edge EXAFS spectrum was taken at a particular spot (POI-2, spectrum Zn-2) and several extended μ-XANES spectra at different places (Fig. 15a). They all had a pronounced dip in the middle of the first oscillation, which is typical of a metal ion (Me = Ni, Zn or Cu) incorporated in the gibbsitic layer of lithiophorite (Fig. 1, Manceau et al., 2000b; Scheinost et al., 2002). This dip arises from the contribution of the nearest Me-Al pair, and its absence when the metal is surrounded by Mn atoms (i.e., incorporated in the MnO_2 layer) is due to the fact that the wave backscattered by Al and Mn atoms are almost out-of-phase (Teo, 1986). This phase contrast translates in distance space by a shift of the imaginary parts of the Me-Al1 and Me-Mn1 pairs, as illustrated in Figure 15b with the Zn- and Ni-data. Notwithstanding the difference of the $\chi_{Zn\text{-}Al1}$ and $\chi_{Zn\text{-}Mn1}$ waves, Figure 15b also shows that Ni and Zn have a similar radial structure function (i.e., similar modulus of the FT) because Ni and Zn both are incorporated in an edge-sharing layer. This illustrates the exquisite sensitivity of EXAFS spectroscopy to the site occupancy of an impurity in a mineral host. To obtain this information, it is important to examine both the magnitude and the phase of the Fourier

transform in real space because the dependence in distance of the FT modulus is essentially determined by the local structure (e.g., type of polyhedral linkages), whereas the imaginary part of the FT provides chemical information (e.g., identity of neighboring atoms).

Zinc was also taken up in the $Al(OH)_3$ layer of lithiophorite in a loess soil from the Mississippi basin (Manceau et al., 2003) and a clayey soil horizon (fragipan) from the Ohio River basin (Manceau et al., 2004), which indicates that the affinity of Zn for gibbsitic layers is a significant geochemical process for Zn sequestration in Earth's near-surface environments. These common structural principles, despite the differing geographical settings and solum properties, are illustrated in Figure 15c,d by the likeness of the Zn μ-EXAFS spectra and Fourier transforms taken in the paddy soil from Taiwan and the soil from Ohio.

3.5. Bulk soil Zn speciation

3.5.1. Powder Zn EXAFS

The dominant form of Zn in the bulk soil was studied by recording the EXAFS spectrum of the homogeneous powder from twenty mottles (Zn-Powder spectrum), and the polarized EXAFS (P-EXAFS) spectra of the self-supporting film from the <0.2 μm soil fraction. The powder and the polarized spectrum at $\alpha = 35°$ (spectrum Zn-35°) have essentially the same shape and frequency; they differ only by the amplitude of the main oscillation (Zn-O pair) at high *k* (Fig. 16a). Spectral analysis showed that the average crystal chemistry of Zn in the bulk soil is well represented by the spectrum of the fine fraction, and since angular measurements are available for this sample, this spectrum will be used below to investigate the dominant form of Zn in the soil. The EXAFS oscillations of the powder and clay samples resemble the μ-EXAFS spectrum of lithiophorite, but are distinct enough to preclude the uptake of Zn in lithiophorite in the fine

soil fraction (Fig. 16b,c). Clearly, Zn is in octahedral coordination in the unknown, because the EXAFS frequency is lower for tetrahedral coordination. Also, the Zn octahedra share edges with Mg or Al octahedra because the first oscillation is split as in lithiophorite. The best spectral matches of the unknown data to our spectral database were obtained with layer minerals containing either of the two low-Z cations (i.e., Mg or Al). A selection of candidate species is shown in Figure 17, and includes Zn-sorbed (spectrum 'Zn-sorbed HIM') and incorporated (spectrum 'Zn-copr. HIM') hydroxy-Al montmorillonite (Roberts et al., 2002; Scheinost et al., 2002), Zn-substituted kerolite (ZnKer003, Zn0.03Mg2.97Si4O10(OH)2·nH2O) from Schlegel et al., 2001), Redhill montmorillonite, SAz-1 montmorillonite (Source Clays Repository of The Clay Minerals Society, [Zn] = 57 mg/kg as measured by ICP-MS), and (Zn,Al)-hydrotalcite (LDH, $Zn_2Al(Kim\ et\ al.)_6[CO_3]_{0.5}$). Each species can be regarded as a 'proxy' for the most likely types of Zn bonding and octahedral linkage: edge-sharing with Al octahedra in the hydroxy-Al species (N_{Al} = 6 Al in Zn-copr. HIM according to Scheinost et al., 2002) and in montmorillonite (N_{Al} = 3), with Mg octahedra in kerolite (N_{Mg} = 6), and with Al and Zn octahedra in hydrotalcite (N_{Al} = 3, N_{Zn} = 3), and in addition corner-sharing linkage with Si tetrahedra in the two layer silicates (N_{Si} = 4). The absorption dip at 3.85 $Å^{-1}$ is deep when Zn is bound to only Al atoms because the amplitude of the Zn-Al1 wave reaches a minimum at this *k* value. The Zn-Si and Zn-Zn waves do not have an amplitude minimum at 3.85 $Å^{-1}$ and when Zn is bonded to several types of cationic shells, the resulting shape of the first oscillation depends on the nature and number of atoms in each shell, as seen in the series of spectra presented in Figure 17. A look at this indicator region in the unknown and the references, and the comparison of Fourier transforms, show obvious likeness with Zn-incorporated hydroxy-Al montmorillonite (the similarity extends to 6 Å in the distance space) and Zn-substituted kerolite, but marked differences with the two natural montmorillonites. This suggests that Zn occupies a vacant site from a dioctahedral $Al(OH)_3$ layer, as in lithiophorite, and not an Al site as in SAz-1 and Redhill montmorillonites (Fig; 1). In other words, Zn has a trioctahedral, and

not a dioctahedral, local structure. This explains the resemblance with low-Zn kerolite since in this mineral Zn octahedra are bonded to six low-Z cations containing octahedra as in a Zn-containing $Al(OH)_3$ layer. The observed differences in the data between kerolite and the hydroxy-Al species, and in particular the lower intensity of the first metal shell peak in the phyllosilicate reference (RSF in Fig. 17c), come from the additional contribution of the four Zn-Si pairs (Si1 shell), whose electronic wave is essentially out-of-phase with that of the six Zn-Mg pairs (Mg1 shell). In the SAz-1 and Redhill montmorillonites, the destructive interference between the Zn-Al1 and Zn-Si1 pairs leads to almost complete extinction of the second RSF peak (Fig. 17 d,e), since in this case Zn has only three nearest octahedral cations (3 Al1), which is not enough to outweigh the contribution from the four Si atoms in the tetrahedral sheet.

3.5.2. Polarized Zn EXAFS

Polarized EXAFS measurements provide further insight into the nature of the Zn-containing aluminous sheet by probing separately the local structure of Zn in the directions perpendicular and parallel to an oriented preparation of the <0.2 μm fraction. The polarization dependence of the EXAFS spectra and Fourier transforms for the Redhill montmorillonite and soil clay films is huge (Fig; 18), in agreement with the high degree of orientation of clay platelets parallel to the substrate plane as measured by texture goniometry. This result indicates that the Zn-containing $Al(OH)_3$ layers are also oriented in the film, as would occur if the gibbsitic and hydrous silicate layers were physically associated. This orientation, the hydroxy-Al nature of the Zn local structure determined by powder EXAFS, and the identification of hydroxy-Al vermiculite by XRD, all collectively suggest that zinc is most likely incorporated in the interlayer of vermiculite. The montmorillonite EXAFS spectrum has a greater angular dependence than the soil sample spectrum because Zn is surrounded by three nearest Al atoms in the film plane and by four Si atoms at higher distance in the perpendicular direction, thus yielding a strongly

anisotropic structural environment. The Si contribution is responsible for the split of the second oscillation, and induces a magnification of the resonance at 5.2 $Å^{-1}$ and a shift to higher *k* values of the oscillation maximum with increasing α angle (Fig. 18b). The angular dependence of the EXAFS spectrum for Zn incorporated in a gibbsitic layer ought to be simpler since Zn has no immediate cationic neighbors in the out-of-plane direction. Accordingly, experimental data show that the second EXAFS oscillation of the soil sample is not split, and that the second RSF peak falls off at $\alpha = 80°$ owing to the absence of a nearest Si shell in the perpendicular direction (Fig. 18 a,c). More insight can be gained from another difference in the data between the montmorillonite and the unknown, mainly the intensity of the second RSF peak which is maximum at $\alpha = 80°$ in montmorillonite (Zn-Si pairs selected) and at $\alpha = 10°$ in the soil sample (Zn-Al pairs selected), and minimum (almost cancelled) at $\alpha = 10°$ in montmorillonite and at α = 80° in the soil sample. In montmorillonite, the Zn-Al pairs are not selected at $\alpha = 10°$ because the projection of the Zn-Si vector on the *ab* plane is not zero, i.e., the E//*ab* signal comes from both the Zn-Al and Zn-Si pairs (for details, see Manceau et al., 1998). In summary, the semi-quantitative interpretation of P-EXAFS data supports our previous interpretation regarding the incorporation of Zn in a gibbsitic layer.

3.5.3. Quantitative data analysis

The first and second RSF peaks of Zn-2, Zn-Powder, Zn-35° and Zn-references spectra were Fourier backtransformed together over the 1.1 to 3.2-3.4 Å $R+\Delta R$ interval and least-squares fitted with two (Zn-O + Zn-Al) or three (Zn-O + Zn-Al + Zn-Si) atomic shells depending on the local structure of Zn in the host phase. A selection of fits to the spectra are shown in Figure 19 and the fit parameters in Table 2. The agreement between theory and data was always satisfactory although the number of shells in the simulations was kept at minimum.

Addition of another shell was never needed to reproduce the data. In montmorillonite, the Si shell comprises two Si atoms at 3.12 Å and two others at 3.18 Å from aluminum (Tsipursky and Drits, 1984). The Si shell coordinated to Ni atoms in Ni-sorbed montmorillonite is also split (Dähn et al., 2003) and, consequently, may also be split around Zn atoms in montmorillonite. This structural hypothesis was tested but the simulation was not significantly improved upon adding a second Zn-Si shell, which we interpret by a decrease of the splitting of the Si1 shell around Zn in montmorillonite in comparison to Al and Ni. Likewise, attempts to add a second oxygen shell at about 3.7 Å in the simulation of the montmorillonite spectrum taken at $\alpha = 10°$ could not be justified statistically, in contrast to Zn-sorbed hectorite (Schlegel et al., 2001). Coordination numbers and interatomic distances obtained by our spectral analysis all agree within errors with known crystallographic values or expected local structure. In particular, Zn appears to be surrounded by 3 Al in the Redhill montmorillonite, indicating that it substitutes for Al and does not fill an empty site from the dioctahedral aluminous sheet. Alternatively, Zn fills an interstitial octahedral site in a gibbsitic layer in lithiophorite, in the two hydroxy-Al phyllosilicate references, and in the clayey soil sample (Zn-35°), as indicated by the doubling of the number of nearest Al neighbors in these minerals relative to montmorillonite. However, a distinction can be made between lithiophorite and the phyllosilicate gibbsitic layer on the basis of the Zn-Al distance, as indicated in the reciprocal space by the shift to higher *k* values of several oscillations of lithiophorite (Fig. 16,bc). Consistently with this observation, spectral simulations showed that the Zn-Al distance is shorter by 0.05 to 0.07 Å in the phyllomanganate compared to the two hydroxy-Al phyllosilicate references and the soil sample, thereby confirming the incorporation of Zn in a gibbsitic layer sandwiched between two TOT phyllosilicate layers in the unknown.

4. DISCUSSION

4.1. Mn^{3+} - Mn^{4+} ordering in lithiophorite

Yang and Wang (2003) reported that manganese has a mean oxidation state of 3.68 in synthetic lithiophorite, indicating that the manganese layer contains about 1/3 Mn^{3+} and 2/3 Mn^{4+} as in TcBi. This value was confirmed in this study by potentiometric titration using $(NH_4)_2Fe(SO_4)\cdot 6H_2O$ Mohr salt and sodium pyrophosphate (Lingane and Karplus, 1946; Vetter and Jaeger, 1966) on our own synthetic lithiophorite sample. Accordingly, its structural formula can be written $(Al_{0.67}Li_{0.32})(Mn^{4+}_{0.68}Mn^{3+}_{0.32})O_2(OH)_2$. The large amount of low valence Mn cations in lithiophorite is also supported by Mn-Mn distances determined by EXAFS and XRD. The Mn-Mn1 and Mn-Mn3 EXAFS distances in lithiophorite (2.91 and 5.86 Å) are greater than those of Mn^{3+}-free dBi (2.87 and 5.74 Å), and similar to the average EXAFS value in TcBi (2.92 and 5.90 Å, Gaillot et al., 2003). In TcBi, the segregation of Mn^{3+} and Mn^{4+} in rows along the *b* axis, together with the collective azimuthal orientation of the elongated Mn^{3+}-O bonds in the *a***c** plane (hexagonal setting), stretches the Mn-Mn distances into the [100] and [110] directions (~2.95 Å) and shortens them into the [010] direction (~2.85 Å, Fig. 11a), thus lowering the symmetry of the MnO_2 layer from hexagonal (as in lithiophorite) to orthogonal ($a \neq b$) (Lanson et al., 2002a). Despite their difference of layer symmetry, lithiophorite and TcBi have almost the same average XRD Mn-Mn distances: d(Mn-Mn1) = 2.925 Å in lithiophorite (Post and Appleman, 1994) and $\langle d(\text{Mn-Mn1})\rangle$ = (2.848 + 2.951 + 2.955)/3 = 2.918 Å in TcBi (Lanson et al., 2002a). The fact that lithiophorite accommodates as much as 1/3 Mn^{3+} in its structure without lowering the symmetry of its MnO_2 layer indicates that Mn^{3+} and Mn^{4+} cations are homogeneously distributed. Using X-ray diffraction it is not possible to determine if Mn^{3+} cations are distributed at random or evenly in the cation array in such a manner that the elongated Mn^{3+}-O bonds are oriented statistically with the same probability in the *ac**, *a***c**, and *bc** planes. This is because in this structural configuration the layer size is increased

uniformly in the [100] and [010] directions and, consequently, $a = b$. Therefore, all the Mn-Mn distances average out to give a constant value (i.e., 2.925 Å) by XRD regardless of the order/disorder of the Mn^{3+}/Mn^{4+} distribution. In contrast, EXAFS spectroscopy is sensitive to the degree of cation order as it gives the local structure around the Mn atom. This is illustrated below with TcBi, followed by a structural model for the ordering of Mn^{3+}/Mn^{4+} in lithiophorite.

In TcBi, the displacement of the two apical oxygens of the Mn^{3+} octahedra due to the Jahn-Teller distortion lengthens the edges of the Mn^{3+}-Mn^{4+} pairs aligned in the [100] and [110] directions, and shortens those from the Mn^{4+}- Mn^{4+} pairs in the [010] direction (hexagonal setting, Fig. 11a). The edges shared by Mn^{3+} octahedra in the [010] direction are not modified. Due to this displacement of oxygen atoms, the Mn^{4+}-Mn^{4+} repulsion is well screened by the two shared oxygens and, consequently, the Mn^{4+}-Mn^{4+} distance is theoretically decreased. In contrast, the Mn^{3+}-Mn^{4+} distance ought to increase to compensate for the lengthening of the shared edges for these two octahedra in agreement with XRD distances. Since Mn^{3+} and Mn^{4+} are ordered in rows along the *b* direction, we see in Figure 11a that the normal (N) Mn^{3+}-Mn^{3+} and short (S) Mn^{4+}-Mn^{4+} distances are all aligned along [010], and the long (L) Mn^{3+}-Mn^{4+} distances are aligned along the [100] and [110] directions. This ordering explains the elongation of the *a* lattice parameter responsible for the departure of the layer from hexagonal symmetry. Also, the layer contains twice as many NLLNLL as NNNNNN and SSSSSS sequences, which is consistent with the split of the Mn1 shell into two Mn atoms at 2.85 Å and four at 2.95 Å as determined by XRD (Lanson et al., 2002a) (Fig. 11a). The split of the Mn-Mn1 distances into two and not three sub-shells indicates that, in reality, the normal (Mn^{3+}-Mn^{3+}) and short (Mn^{4+}-Mn^{4+}) distances are similar despite the shorter length of the Mn^{4+}-Mn^{4+} shared edge.

The structural model proposed for the distribution of Mn^{3+} and Mn^{4+} in the MnO_2 layer of lithiophorite was built with the following constraints: the layer contains 1/3 Mn^{3+}, its symmetry is hexagonal, and the Mn shells are split as in TcBi (Fig. 11a). The hexagonal symmetry of the MnO_2 layer can be preserved by rotating the azimuthal orientation of the Mn^{3+} octahedra by 0°,

+60°, and –60° with equal probability, and the split of the Mn-Mn distances can be preserved by forbidding Mn^{3+}-Mn^{3+} pairs. The sequences of shared-edges along the [100], [010], and [110] directions are now NNNNNN and SLLSLL, with the latter being twice that of the former, meaning that the local distortion is preserved. However, we see in Figure 11a that the three directions are now equivalent since the two sequences have the same periodicity in all directions, thus imparting to the MnO_2 layer a hexagonal symmetry.

According to the structural model in Fig. 11a, the splitting of the Mn-Mn1 and Mn-Mn3 distances should be smaller in lithiophorite than in TcBi because Mn^{3+} cations are homogeneously distributed in the former species. This inference is supported experimentally since the EXAFS separation in distance of Mn atoms in the Mn1 shell is 0.11 Å for TcBi (Gaillot et al., 2003), in agreement with XRD (0.10 Å), and lower and below the resolution limit of EXAFS for lithiophorite (0.07 Å). The split of the Mn3 shell is 0.21 Å by EXAFS and 0.20 Å by XRD in TcBi, whereas it is only 0.14 Å in lithiophorite. Finally, indirect support for this model comes from the likeness of the distribution pattern of inequivalent octahedra in the MnO_2 and $Al(OH)_3$ layers of lithiophorite, since the vacant sites of the gibbsitic layer have the same distribution as Mn^{3+} in the manganiferous layer, and from the presence of superstructure reflections observed by X-ray diffraction (Post and Appleman, 1994). The gibbsitic layer of lithiophorite is positively charged owing to the incorporation of lithium and various divalent foreign cations (Cu^{2+}, Zn^{2+}) in the vacant sites of the dioctahedral layer, and this charge is compensated in the manganese layer by the substitution of Mn^{3+} for Mn^{4+} cations. Consequently, heterovalent cations (Mn^{3+}, Li^{+}, Cu^{2+}, Zn^{2+}…) with the same distribution pattern in the two layers likely increases the overall stability of the mineral by providing a more homogeneous and local balance of the excess and deficit of charges in each layer.

4.2. Ni and Zn site occupancy in lithiophorite

Natural lithiophorites are generally depleted in lithium and enriched in trace metals, including Cu, Ni, Zn, and Co (Ostwald, 1988). The chemical variability of lithiophorite is reflected by the diversity of empirical formulae that have been advanced, for example, $Li_2Al_8(Mn^{2+},Co,Ni)_2Mn_{10}^{4+}O_{35}\cdot 14H_2O$ (Fleischer and Richmond, 1943), $(Al,Li)(Mn_{0.82}^{4+}Mn_{0.17}^{2+})O_2(OH)_2$ (Wadsley, 1952), $Li_2Al_8Mn_{12}O_{35}\cdot 14H_2O$ (Wagner et al., 1979), and $(Al_4Li_2)(Mn_5^{4+}Mn^{2+})O_{12}(OH)_{12}$ (Giovanoli et al., 1973). A survey of published chemical analyses shows that the Li content can be as low as 0.04 wt. %, and as high as 3.3 wt. % in specimen lacking trace metals (Mitchell and Meintzer, 1967; Ostwald, 1984b; Ostwald, 1988). It has been generally assumed that Ni^{2+} (0.70 Å), Cu^{2+} (0.73 Å) and Zn^{2+} (0.74 Å) fill the vacant site of the gibbsitic layer because they are a close match in size for Li^{+} (0.74 Å) (Wagner et al., 1979). Zinc is clearly too big to substitute for Al (0.53 Å), Mn^{4+} (0.54 Å), and Mn^{3+} (0.65 Å) and, for steric reasons, it can enter only the Li site. This hypothesis was verified previously on natural lithiophorite from a pristine horizon of a clayey soil in Ohio (Manceau et al., 2004) and on a banded Mn ore deposit from the Ivory Coast (Manceau et al., 1990), and is confirmed in the present study on a paddy soil. In terms of size, Ni^{2+} is also a good fit for isomorphic substitution of Mn^{3+} (0.65 Å). It has been shown by EXAFS that nickel is incorporated into the manganese layer of lithiophorite in soil, a finding which is confirmed also in the present study (Manceau et al., 2002b). However, nickel was found to be in the gibbsitic layer in lithiophorite from lateritic profiles on ultrabasites deposits from New Caledonia (Manceau et al., 1987). Therefore, it is possible that the incorporation mechanism of nickel depends on the stoichiometry of the natural lithiophorite and its formation condition. When conditions permit (e.g., availability of a vacant site in the MnO_2 layer), the smaller size of the Mn^{3+} site relative to the Li site probably favors the manganese site preference for Ni, for energetic reasons.

4.3. Zn speciation in Al-hydroxy vermiculite

Zinc is predominantly associated with phyllosilicate in the paddy soil. The combination of XRD and powder and polarized EXAFS measurements indicates that Zn is contained in hydroxy-Al layers intercalated between the 2:1 layers of vermiculite. The Zn^{2+} cations fill the vacant sites of the dioctahedral Al hydroxide layers and, consequently, provide the excess positive charge required to balance the negative charge from the 2:1 layers. Theoretically, some Zn atoms could go in the 2:1 octahedral sheet where they would be closer to the source of negative charge, but they do not. The interlayer sheet requires an overall positive charge for its stability between two negatively charged 2:1 layers, and this is provided by the incorporation of Zn^{2+} in the vacant octahedral sites of the $Al(OH)_3$ interlayer, in a similar manner to that in lithiophorite. Consequently, the two identified Zn species reduce to one at the molecular scale, in the sense that Zn has the same binding environment in the two host phases, the difference lying in the fact that the Zn-containing gibbsitic layer is sandwiched between MnO_2 layers in lithiophorite and 2:1 layers in the phyllosilicate. Although Zn has the same coordination chemistry in the two soil species, differentiation is possible by EXAFS on the basis of Zn-Al distances which are shorter in lithiophorite (~3.01 Å) than in the phyllosilicate (~3.06 - 3.07 Å), as shown by the lower frequency of the lithiophorite spectrum (Fig. 16b). Obviously, chemical analysis by μ-SXRF and solid phase identification by μ-XRD afford other means to differentiate these two species at the micrometer-scale.

This hydroxy-Al Zn species was described for the first time by powder EXAFS spectroscopy in a smelter-affected acidic soil (pH 3.9) at Palmerton, Pennsylvania (Scheinost et al., 2002), and was subsequently found in the fragipan horizon (pH 4.5 - 5.0) of the Ohio soil mentioned previously. In the present study, the application of polarized EXAFS demonstrated that the gibbsitic layers hosting zinc were oriented parallel to the phyllosilicate layers during the preparation of the self-supporting film, which is a strong argument in support of the physical intercalation of the two types of layers. Another piece of evidence comes from the abundance of

hydroxy-Al vermiculite by X-ray diffraction. This hydroxy-Al phyllosilicate Zn species is probably widespread in acidic soils, and in particular in Ultisols owing to the abundance of vermiculite is these soils (Hseu et al., 2004; Li et al., 1998). This species seems to occur together with lithiophorite, as this latter was identified also in the Pennsylvannia and Ohio soils. The co-existence of these two species may be explained by the fact that they both form in acidic conditions (Barnhisel and Bertsch, 1982; Taylor et al., 1964) and can be prepared in the laboratory by the intercalation and polymerization of aluminium in the interlayer space of phyllosilicate and birnessite (Feng et al., 1999; Furrer et al., 2001). Finally, the similarity of the structural environment in lithiophorite and vermiculite (i.e., similar Zn affinity and partitioning), together with the abundance and uniform distribution of phyllosilicate in the soil (vermiculite is present in the soil matrix and in soft mottles) account for the smaller Zn than Ni partitioning in soil ferromanganese nodules over the clayey matrix found in this study (Table 1, Fig. 1), and reported in the literature (Childs, 1975; Palumbo et al., 2001).

Acknowledgment - The authors acknowledge comments from the anonymous reviewers. J.L. Hazemann and O. Proux are thanked for their assistance during EXAFS measurements on FAME (ESRF). The ALS and the CNRS, which supports the French-CRG program at ESRF, are acknowledged for the provision of beamtime. The texture goniometry equipment was funded by the *Délégation Régionale à la Recherche et à la Technologie - Basse-Normandie*. A.M. and S.R. thank the GdR-TRANSMET from the CNRS for funding this research. The ALS is supported by the Director, Office of Energy Research, Office of Basic Energy Sciences, Materials Sciences Division of the U.S. Department of Energy, under Contract No. DE-AC03-76SF00098.

REFERENCES

Ahrens L. H., Willis J. P., and Oosthuizen C. O. (1967) Further observations on the composition of manganese nodules, with particular reference to some of the rarer elements. *Geochim. Cosmochim. Acta* **31**, 2169-2180.

Baize D. and Chrétien J. (1994) Les couvertures pédologiques de la plate-forme sinémurienne en Bourgogne: particularités morphologiques et pédo-géochimiques. Etude et Gestion des Sols **2**, 7-27.

Barnhisel R. and Bertsch P. M. (1982) Aluminum. In *Methods of Soil Analysis, Part 2, Chemical and Microbiological Properties* (ed. A. L. Page), pp. 288-290. Soil Sci. Soc. Amer.

Bidoglio G., Gibson P. N., Haltier E., Omenetto N., and Lipponen M. (1992) XANES and laser fluorescence spectroscopy for rare earth speciation at mineral-water interfaces. *Radiochim. Acta* **58**, 191-197.

Boudeulle M. and Muller J. P. (1988) Structural characteristics of hematite and goethite and their relationships with kaolinite in a laterite from Cameroon . A TEM study. *Bull. Miner.* **111**, 149-166.

Chen Z. S., Tsou T. C., Asio V. B., and Tsai C. C. (2001) Genesis of inceptisols on a volcanic landscape in Taiwan. *Soil Sci.* **166**, 255-266.

Childs C. W. (1975) Composition of iron-manganese concretions from some New Zealand soils. *Geoderma* **13**, 141-152.

Chukhrov F. V. and Gorshkov A. I. (1981) Iron and manganese oxide minerals in soils. *Trans. of Royal Soc., Edinburg* **72**, 195-200.

Chukhrov F. V., Gorshkov A. I., Sivtsov A. V., and Berezovskaya V. V. (1985) The nature and genesis of lithiophorite. *Int. Geol. Rev.* **27**, 348-361.

Dähn R., Scheidegger A. M., Manceau A., Schlegel M. L., Baeyens B., Bradbury M. H., and Chateigner D. (2003) Structural evidence for the sorption of metal ion on the edges of montmorillonite layers. A polarized EXAFS study. *Geochim. Cosmochim. Acta* **67**, 1-15.

Dawson B. S. W., Fergusson J. E., Campbell A. S., and Cutler E. J. B. (1985) Distribution of elements in some Fe-Mn nodules and an iron-pan in some gley soils of New-Zeland. *Geoderma* **35**, 127-143.

De Carlo E. H. and McMurtry G. M. (1992) Rare-earth element geochemistry of ferromanganese crusts from the Hawaiian Archipelago, central Pacific. *Chem. Geol.* **95**, 235-250.

Douglas L. A. (1989) Vermiculites. In *Minerals in Soil Environments* (eds. J. B. Dixon and S. B. Weed), pp. 635-728. Soil Sci. Soc. Amer., Madison, WI.

Drits V. A., Lanson B., Bougerol-Chaillout C., Gorshkov A. I., and Manceau A. (2002) Structure of heavy metal sorbed birnessite. Part 2. Results from electron diffraction. *Am. Mineral.* **87**, 1646-1661.

Drits V. A., Silvester E., Gorshkov A. I., and Manceau A. (1997) The structure of synthetic monoclinic Na-rich birnessite and hexagonal birnessite. Part 1. Results from X-ray diffraction and selected area electron diffraction. *Am. Mineral.* **82**, 946-961.

Feng Q., Horiuchi T., Liu L.H., Yanagisawa K., and Mitsushio T. (1999) Hydrothermal soft chemical reaction for formation of sandwich layered manganese oxide. *Chem. Mater.* **11**, 2444-2450.

Fleischer M. and Richmond W. E. (1943) The manganese oxide minerals: a preliminary report. *Econ. Geol.* **38**, 269-286.

Fukuda T., Nagasaki S., Satta H., Tanaka S., Suzuki A., Tanaka T., and Muraoka S. (1998) Adsorption/desorption of lanthanides on metal oxides interfaces. *Radiochim Acta* **82**, 239-242.

Furrer G., Scheidegger A., Plötze M., Kahr G., Studer B., Lothenbach B., and Schulin R. (2001) Specific immobilization of heavy metals in soil using modified montmorillonite. *Mitt. Dtsch. Bodenkundl. Ges.* **96**, 181-182.

Gaillot A. C., Flot D., Drits V. A., Burghammer M., Manceau A., and Lanson B. (2003) Structure of synthetic K-rich birnessites obtained by high-temperature decomposition of KMnO4. I. Two-layer polytype from a 800°C experiment. *Chem. Mater.* **15**, 4666-4678.

Giovanoli R., Buhler H., and Sokolowska K. (1973) Synthetic lithiophorite: electron microscopy and X-ray diffraction. *J. Microsc.* **18**, 271-284.

Gromet L. P., Dymek R. F., Haskin L. A., and Korotev R. L. (1984) The 'North American shale composite': Its compilation, major and trace element characteristics. *Geochim. Cosmochim. Acta* **48**, 2469-2481.

Guilmeau E., Funahashi R., Mikami M., Chong K., Chateigner D. (2004) Thermoelectric properties–texture relationship in highly oriented $Ca_3Co_4O_9$ composites. *Applied Physics Letters* **85**, 1490-1492

Hseu Z. Y. and Chen Z. S. (1996) Saturation, reduction, and redox morphology of seasonally flooded Alfisols in Taiwan. *Soil Sci. Soc. Amer. J.* **60**, 941-949.

Hseu Z. Y. and Chen Z. S. (1997) Soil hydrology and micromorphology of illuvial clay in an Ultisol hydrosequence. *J. Chinese Agricul. Chem. Soc.* **35**, 503-512.

Hseu Z. Y. and Chen Z. S. (1999) Micromorphology of redoximorphic features of subtropical anthraquic Ultisols. *Food Science and Agricultural Chemistry* **1**, 194-202.

Hseu Z.Y and Chen Z.S. (2001) Quantifying soil hydromorphology of a rice-growing ultisol toposequence in Taiwan. *Soil Sci. Soc. Amer. J.* **65**, 270-278.

Hseu Z. Y., Tsai C. C., Lin C. W., and Chen Z. S. (2004) Transitional soil characteristics between Ultisols and Spodosols in the Subalpine Forest of Taiwan. *Soil Sci.* **169**, 457-467.

Isaure M. P., Laboudigue A., Manceau A., Sarret G., Tiffreau C., Trocellier P., Hazemann J. L., and Chateigner D. (2002) Quantitative Zn speciation in a contaminated dredged sediment by

μPIXE, μSXRF, EXAFS spectroscopy and principal component analysis. *Geochim. Cosmochim. Acta* **66**, 1549-1567.

Isaure M. P., Manceau A., Geoffroy N., Laboudigue A., Tamura N., and Marcus M. A. (2005) Zinc mobility and speciation in soil covered by contaminated dredged sediment using micrometer-scale and bulk-averaging X-ray fluorescence, absorption and diffraction techniques. *Geochim. Cosmochim. Acta*, in press.

Jeffery G.B. (1923) The motion of ellipsoidal particles immersed in a viscous fluid. *Proc. Royal. Society of London* **A102**, 161-179.

Juillot F., Morin G., Ildefonse P., Trainor T. P., Benedetti M., Galoisy L., Calas G., and Brown G. E. (2003) Occurrence of Zn/Al hydrotalcite in smelter-impacted soils from northern France: Evidence from EXAFS spectroscopy and chemical extractions. *Am. Mineral.* **88**, 509-526.

Kabata-Pendias A. (1980) Heavy metals sorption by clay minerals and oxides or iron and manganese. *Mineral. Polonica* **11**, 3-13.

Kasten S., Glasby G. P., Schulz H. D., Friedrich G., and Andreev S. I. (1998) Rare earth elements in manganese nodules from the South Atlantic Ocean as indicators of oceanic bottom water flow. *Marine Geol.* **146**, 33-52.

Koschinsky A. and Hein J. R. (2003) Uptake of elements from seawater by ferromanganese crusts: solid-phase associations and seawater speciation. *Marine Geol.* **198**, 331-351.

Lanson B., Drits V. A., Feng Q., and Manceau A. (2002a) Crystal structure determination of synthetic Na-rich birnessite: Evidence for a triclinic one-layer cell. *Am. Mineral.* **87**, 1662-1671.

Lanson B., Drits V. A., Gaillot A. C., Silvester E., Plançon A., and Manceau A. (2002b) Structure of heavy metal sorbed birnessite. Part 1. Results from X-ray diffraction. *Am. Mineral.* **87**, 1631-1645.

Latrille C., Elsass F., van Oort F., and Denaix L. (2001) Physical speciation of trace metals in Fe-Mn concretions from a rendzic lithosol developed on Sinemurian limestones (France). *Geoderma* **100**, 127-146.

Li S. Y., Chen Z. S., and Liu J. C. (1998) Subalpine loamy Spodosols in central Taiwan: Characteristics, micromorphology, and genesis. *Soil Sci. Soc. Am. J.* **62**, 710-716.

Li Y. H. (1982) Interelement relationship in abyssal Pacific ferromanganese nodules and associated pelagic sediments. *Geochim. Cosmochim. Acta* **46**, 1053-1060.

Lingane J. J. and Karplus R. (1946) New Method for Determination of Manganese. *Indust. Engin. Chem.. Anal. Ed.* **18**, 191-194.

Lutterotti L., Chateigner D., Ferrari S., Ricote J. (2004) Texture, residual stress and structural analysis of thin films using a combined X-ray analysis. *Thin Solid Films* **450**, 34-41.

Malla P. B. and Douglas L. A. (1987) Identification of expanding layer silicates: Charge density vs. expansion properties. In *Proceedings of the International Clay Conference, Denver* (eds. L.G. Schultz, H. van Olphen, and F. A. Mumpton), pp. 277-283. The Clay Minerals Society.

Manceau A., Llorca S., and Calas G. (1987) Crystal chemistry of cobalt and nickel in lithiophorite and asbolane from New Caledonia. *Geochim. Cosmochim. Acta* **51**, 105-113.

Manceau A., Bonnin D., Kaiser P., and Frétigny C. (1988) Polarized EXAFS of biotite and chlorite. *Phys. Chem. Mineral.* **16**, 180-185.

Manceau A. and Combes J. M. (1988) Structure of Mn and Fe oxides and oxyhydroxides: a topological approach by EXAFS. *Phys. Chem. Mineral.* **15**, 283-295.

Manceau A., Rask J., Buseck P. R., and Nahon D. (1990) Characterization of copper in lithiophorite from a Mn banded ore. *Am. Mineral.* **75**, 490-494.

Manceau A., Gorshkov A. I., and Drits V. A. (1992) Structural chemistry of Mn, Fe, Co, and Ni in Mn hydrous oxides. II. Information from EXAFS spectroscopy, electron and X-ray diffraction. *Am. Mineral.* **77**, 1144-1157.

Manceau A., Drits V. A., Silvester E., Bartoli C., and Lanson B. (1997) Structural mechanism of Co(II) oxidation by the phyllomanganate, Na-buserite. *Am. Mineral.* **82**, 1150-1175.

Manceau A., Chateigner D., and Gates W. P. (1998) Polarized EXAFS, distance-valence least-squares modeling (DVLS) and quantitative texture analysis approaches to the structural refinement of Garfield nontronite. *Phys. Chem. Mineral.* **25**, 347-365.

Manceau A., Lanson B., Schlegel M. L., Hargé J. C., Musso M., Eybert-Bérard L., Hazemann J. L., Chateigner D., and Lamble G. M. (2000a) Quantitative Zn speciation in smelter-contaminated soils by EXAFS spectroscopy. *Amer. J. Sci.* **300**, 289-343.

Manceau A., Schlegel M. L., Musso M., Sole V. A., Gauthier C., Petit P. E., and Trolard F. (2000b) Crystal chemistry of trace elements in natural and synthetic goethite. *Geochim Cosmochim. Acta* **64**, 3643-3661.

Manceau A. and Schlegel M. L. (2001) Texture effect on polarized EXAFS amplitude. *Phys. Chem. Mineral*. **28**, 52-56.

Manceau A., Marcus M. A., and Tamura N. (2002a) Quantitative speciation of heavy metals in soils and sediments by synchrotron X-ray techniques. In *Applications of Synchrotron Radiation in Low-Temperature Geochemistry and Environmental Science*, Vol. 49 (eds. P. A. Fenter, M. L. Rivers, N. C. Sturchio, and S. R. Sutton), pp. 341-428. Miner. Soc. Amer., Washington DC.

Manceau A., Tamura N., Marcus M. A., MacDowell A. A., Celestre R. S., Sublett R. E., Sposito G., and Padmore H. A. (2002b) Deciphering Ni sequestration in soil ferromanganese nodules by combining X-ray fluorescence, absorption and diffraction at micrometer scales of resolution. *Am. Mineral.* **87**, 1494-1499.

Manceau A., Tamura N., Celestre R. S., MacDowell A. A., Geoffroy N., Sposito G., and Padmore H. A. (2003) Molecular-scale speciation of Zn and Ni in soil ferromanganese nodules from loess soils of the Mississippi basin. *Environ. Sci. Technol.* **37**, 75-80.

Manceau A., Marcus M. A., Tamura N., Proux O., Geoffroy N., and Lanson B. (2004) Natural speciation of Zn at the micrometer scale in a clayey soil using X-ray fluorescence, absorption, and diffraction. *Geochim. Cosmochim. Acta* **68**, 2467-2483.

Marcus M.A., MacDowell A. A., Celestre R., Manceau A., Miller T., Padmore H. A., and Sublett R. E. (2004a) Beamline 10.3.2 at ALS: a hard X-ray microprobe for environmental and materials sciences. *J. Synch. Rad.* **11**, 239-247.

Marcus M. A., Manceau A., and Kersten M. (2004b) Mn, Fe, Zn and As speciation in a fast-growing ferromanganese marine nodule. *Geochim. Cosmochim. Acta* **68**, 3125-3136.

Marques J. J., Teixeira W. G., Schulze D. G., and Curi N. (2002) Mineralogy of soils with unusually high exchangeable Al from the western Amazon Region. *Clay Mineral.* **37**, 651-661.

McKenzie R. M. (1972) The manganese oxides in soils. A review. *Zeitschrift fur Pflanzenernahrung und Bodenkunde,* 221-242.

Mitchell R. S. and Meintzer R. E. (1967) Lithiophorite from Charlottesville, Virginia. *Am. Mineral.* **52**, 1545-1549.

Moore D. M. and Reynolds R. C. J. (1997) *X-ray diffraction and the Identification and Analysis of Clay Minerals*. Oxford University Press.

Ohta A. and Kawabe I. (2001) REE(III) adsorption onto Mn dioxide (δ-MnO_2) and Fe oxyhydroxide: Ce(III) oxidation by δ-MnO_2. *Geochim. Cosmochim. Acta* **65**, 695-703.

O'Reilly S. E. and Hochella M. F. (2003) Lead sorption efficiencies of natural and synthetic Mn and Fe-oxides. *Geochim. Cosmochim. Acta* **67**, 4471-4487.

Ostergren J. D., Brown G. E., Parks G. A., and Tingle T. N. (1999) Quantitative lead speciation in selected mine tailings from Leadville, CO. *Environ. Sci. Technol.* **33**, 1627-1636.

Ostwald J. (1984a) Ferruginous vernadite in an Indian ocean ferromanganese nodule. *Geol. Mag.* **121**, 483-488.

Ostwald J. (1984b) Two varieties of lithiophorite in some Australian deposits. *Mineral Mag.* **48**, 383-388.

Ostwald J. (1988) Mineralogy of the Groote Eylandt manganese oxides: A review. *Ore Geology Reviews* **4**, 3-45.

Palumbo B., Bellanca A., Neri R., and Roe M. J. (2001) Trace metal partitioning in Fe-Mn nodules from Sicilian soils, Italy. *Chem Geol* **173**, 257-269.

Panfili F., Manceau A., Sarret G., Spadini L., Kirpichtchikova T., Bert V., Laboudigue A., Marcus M. A., Ahamdach N., and Libert M. F. (2005) The effect of phytostabilization on Zn speciation in a dredged contaminated sediment using scanning electron microscopy, X-ray fluorescence, EXAFS spectroscopy and principal components analysis. *Geochim. Cosmochim. Acta*, in press.

Post J. E. and Appleman D. E. (1994) Crystal structure refinement of lithiophorite. *Am. Mineral.* **79**, 370-374.

Ressler T. (1998) WinXAS: a Program for X-ray Absorption Spectroscopy Data Analysis under MS-Windows. *J. Synchr. Rad.* **5**, 118-122.

Richardson S. M. and Richardson J. W. (1982) Crystal structure of a pink muscovite from Archer's post, Kenya: implications for reverse pleochroism in dioctahedral micas. *Am. Mineral.* **67**, 69-75.

Roberts D. R., Scheinost A. C., and Sparks D. L. (2002) Zinc speciation in a smelter-contaminated soil profile using bulk and microscopic techniques. *Environ. Sci. Technol.* **36**, 1742-1750.

Ruiz J. M., Delgado A., and Torrent J. (1997) Iron-related phosphorus in overfertilized European soils. *J. Environ. Qual.* **26**, 1548-1554.

Scheinost A. C., Kretzschmar R., Pfister S., and Roberts D. R. (2002) Combining selective sequential extractions, X-ray absorption spectroscopy and principal component analysis for quantitative zinc speciation in soil. *Environ. Sci. Technol.* **36**, 5021-5028.

Schlegel M. L., Manceau A., Charlet L., and Hazemann J. L. (2001) Adsorption mechanism of Zn on hectorite as a function of time, pH, and ionic strength. *Amer. J. Sci.* **301**, 798-830.

Scott K. M. (1987) Significance of a lithiophorite interface between cryptomelane and florencite. *Am. Mineral.* **72**, 429-432.

Stolt M. H., Ogg C. M., Baker J. C. (1994) Strongly contrasting redoximorphic patterns in Virginia Valley and Ridge paleosols. *Soil Sci. Soc. Am. J.* **58**, 477-484.

Southard R. J. and Buol S. W. (1988) Subsoil blocky structure formation in some North Carolina Paleudults and Paleaquults. *Soil Sci. Soc. Am. J.* **52**, 1069-1076.

Stiles C. A., Mora C. I., and Driese S. G. (2001) Pedogenic iron-manganese nodules in Vertisols: A new proxy for paleoprecipitation? *Geology* **29**, 943-946.

Sutton S. R., Bertsch P. M., Newville M., Rivers M., Lanzirotti A., and Eng P. (2002) Microfluorescence and microtomography analyses of heterogeneous earth and environmental materials. In *Applications of Synchrotron Radiation in Low-Temperature Geochemistry and Environmental Science*, Vol. 49 (eds. P. A. Fenter, M. L. Rivers, N. C. Sturchio, and S. R. Sutton), pp. 429-478. Miner. Soc. Amer., Washington DC.

Syers J. F., Harris R. F., and Armstrong D. E. (1973) Phosphate chemistry in lake sediments. *J. Environ. Qual.* **2**, 1-14.

Takahashi Y., Shimizu H., Kagi H., Yoshida H., Usui A., and Nomura M. (2000) A new method for the determination of CeIII/CeIV ratios in geological materials; application for weathering, sedimentary and diagenetic processes. *Geophys. Res. Lett.* **182**, 201-207.

Taylor R. M. (1968) The association of manganese and cobalt in soils- further observations. *J. Soil Sci.* **19**, 77-80.

Taylor R. M. and McKenzie R. M. (1966) The association of trace elements with manganese minerals in Australian soils. *Australian J. Soil Res.* **4**, 29-39.

Taylor R. M., McKenzie R. M., and Norrish K. (1964) The mineralogy and chemistry of manganese in some Australian soils. *Australian J. Soil Res.* **2**, 235-248.

Teo B. K. (1986) *EXAFS: basic principles and data analysis*. Springer-Verlag.

Tsipursky S. I. and Drits V. A. (1984) The distribution of cations in the 2:1 layers of dioctahedral smectites studied by oblique-texture electron diffraction. *Clay Mineral.* **19**, 177-193.

Uzochukwu G. A. and Dixon J. B. (1986) Manganese oxide minerals in nodules of two soils of Texas and Alabama. *Soil Sci. Soc. Am. J.* **50**, 1358-1363.

Vaniman D. T., Chipera S. J., Bish D. L., Duff M. C., and Hunter D. B. (2002) Crystal chemistry of clay-Mn oxide associations in soils, fractures, and matrix of the Bandelier Tuff, Pajarito Mesa, New Mexico. *Geochim. Cosmochim. Acta* **66**, 1349-1374.

Varentsov I. M., Drits V. A., Gorshkov A. I., Sivtsov A. V., and Sakharov B. A. (1991) Me-Fe oxyhydroxide crusts from Krylov Seamount (Eastern Atlantic): Mineralogy, geochemistry and genesis. *Marin. Geol.* **96**, 53-70.

Vepraskas M. J. and Wilding L. P. (1983) Albic neoskeletans in argillic horizons as indices of seasonal saturation and iron reduction. *Soil Sci. Soc. Am. J.* **47**, 1202-1207.

Vetter K. J. and Jaeger N. (1966) Potentialausbildung an der Mangan-dioxid-elektrode als Oxidelektrode mit nichtstöchiometrischem Oxid. *Electrochim. Acta* **11**, 401-419.

Vodyanitskii Y. N., Gorshkov A. I., and Sivtsov A. V. (2002) Peculiarities of manganese oxides in soils of the Russian Plain. *Eurasian Soil Sci.* **35**, 1037-1045.

Wadsley A. D. (1952) The structure of lithiophorite, $(Al,Li)MnO_2(OH)_2$. *Acta Cryst.* **5**, 676-680.

Wagner G. H., Konig R. H., Vogelpohl S., and Jones M. D. (1979) Base metals and other minor elements in the manganese deposits of West-Central Arkansas. *Chem. Geol.* **27**, 309-327.

Yang D. S. and Wang M. K. (2003) Characterization and a fast method for synthesis of sub-micron lithiophorite. *Clays Clay Mineral.* **51**, 96.

Zabinsky S. I., Rehr J. J., Ankudinov A., Albers R. C., and Eller M. J. (1995) Multiple scattering calculations of X-ray absorption spectra. *Phys. Rev.* **52**, 2995-3009.

FIGURE CAPTION

Fig. 1. Schematic representation of the site occupancy of Zn in lithiophorite, Zn-substituted montmorillonite, Zn-substituted kerolite, and hydroxy-Al phyllosilicate.

Fig. 2. Concentration of major and trace elements in the four ferruginous mottles and in the ferromanganiferous mottle (a), and enrichment factor (EF) for each element relative to the soil matrix (b). EF is defined as the ratio of the element concentration in mottle over the element concentration in the surrounding soil (Ahrens et al., 1967). The vertical bars are the standard variations calculated from the analyses of the four Fe mottles.

Fig. 3. XRD patterns collected on oriented preparations of the < 0.2 μm soil size fraction. a) Mg-saturated mount in the air-dried state (Mg) and after ethylene glycol (EG) and glycerol (G) solvation. b) K-saturated mount (K) after *ex situ* thermal treatment. Cl : chlorite, M : illite/mica, Ka : ordered kaolinite, dKa : disordered kaolinite, V : vermiculite, I : interstratified illite/mica – vermiculite, A : albite, Mi : microcline, Gt : goethite, Q : quartz, Hy : Hydroxy-Al vermiculite.

Fig. 4. XRD diagrams for the textured <0.2 μm soil clay fraction (a) and the textured <2 μm fraction of Redhill montmorillonite (b). M: mica, Ka: kaolinite, L: lepidocrocite, I : interstratified illite/mica – vermiculite, Q: Quartz..

Fig. 5. Pseudo 3D diagram of the soil clay film centred on the 002 reflections of mica and illite/mica - vermiculite. The pseudo axis varies from $\rho = 0°$ (back) to 30° (front) by steps of 5°.

Fig. 6. Radial distribution density profiles of the 002-mica (a), 002-interstratified phase (b), 020-lepidocrocite (c), and 001-kaolinite (d) reflections for the soil clay film, and of the 001-montmorillonite reflection for the Redhill montmorillonite (e).

Fig. 7. Two-color (RG) and tricolor (RGB) μ-SXRF maps of a Fe-Mn mottle. Red codes for Zn and Ni, green for Fe, and blue for Mn. Each pixel is colored in proportion to the Ni Kα, Zn Kα, Mn Kα, and Fe Kβ signal. a) Coarse map of a 3800 H x 2800 V μm^2 area representative of the entire nodule, recorded at 15 x 15 μm resolution. b) and c) Fine maps from two regions of the coarse map. b) Size = 2100 H x 1800 V μm, resolution = 9 x 9 μm. c) Size = 1400 H x 650 V μm, resolution = 7 x 7 μm. The numbers indicate the spots where μ-XRD patterns and μ-EXAFS spectra were collected.

Fig. 8. X-ray fluorescence spectrum averaged over all pixels from the coarse map (i.e., taken while recording the map) (a), and XRF spectra from selected spots on the μ-SXRF maps (b-e). Incident X-ray energy = 10 keV. Dotted line: linear scale; solid line : logarithmic scale.

Fig. 9. One-dimensional μ-XRD patterns (λ = 2.066 Å) from selected spots on the μ-SXRF maps obtained from two-dimension patterns by integrating intensities at constant Bragg angle. A: anatase, Al: albite, B: turbostratic hexagonal birnessite (Fe-vernadite), F: feldspath, FeOx: poorly-crystalline Fe (oxyhydr)oxide (Mn-feroxyhite), G: goethite, H: hematite, L: lepidocrocite, Li: lithiophorite, P: phyllosilicate, Q: quartz. The relative intensity of the *hkl* reflections for the coarse grains are different from the powder pattern of the same mineral species because only a few individual crystals satisfy the Bragg condition in μ-XRD experiment.

Fig. 10. Mn K-edge μ-EXAFS collected at spot 1 (Mn-1) and 4 (Mn-4) and powder spectrum for synthetic lithiophorite (Lit, $(Al_{0.67}Li_{0.32})(Mn^{4+}_{0.68}Mn^{3+}_{0.32})O_2(OH)_2$) and birnessite references. Triclinic birnessite (TcBi) has 31 % Mn^{3+}, the turbostratic hexagonal birnessite dBi-1 has nil Mn^{3+}, and the turbostractic hexagonal birnessite dBi-2 has 21 % Mn^{3+}. The EXAFS for the references have been multiplied by 0.58 in b-d) to account for overabsorption of the fluorescence-yield sample spectra. Vertical lines in e) are at 7.9, 8.05, 8.9, 9.0, 9.2, 11.4 and 11.6 $Å^{-1}$.

Fig. 11. a) Schematic representation of the distribution of Mn^{3+} and Mn^{4+} cations in the manganese layer of triclinic birnessite (TcBi) and lithiophorite. b) Mn-Mn distances for the first (Mn1), third (Mn3), and fifth (Mn5) Mn shells in triclinic birnessite (Lanson et al., 2002a). These shells have their EXAFS contribution reinforced by multiple scattering effect owing to the alignment of Mn atoms.

Fig. 12. Modulus and imaginary part of the Fourier transform for synthetic lithiophorite compared to those of hexagonal birnessite with only Mn^{4+} and no interlayer Mn (dBi-1) and triclinic birnessite with 31 % Mn^{3+} and no interlayer Mn (TcBi). The two arrows show the splitting of the Mn-Mn distances in the third Mn shell of lithiophorite and triclinic birnessite.

Fig. 13. Inverse Fourier transform of the synthetic lithiophorite, dBi-1 and TcBi data in the [2.1 - 3.1 Å] interval (Mn1 shell) (a,b), and in the [4.9 - 5.9 Å] interval (Mn3 shell) (c,d) with spectral simulations (e,f). In e,f), the data are in solid lines, and the models in dotted lines.

Fig. 14. Ni K-edge μ-EXAFS collected at spot 1 and Fourier transform (Ni-1) compared to reference data in which Ni is substituted for Mn in the manganese layer of a soil lithiophorite (after Manceau et al., 2002b).

Fig. 15. a,b) Ni (Ni-1) and Zn (Zn-2) K-edge μ-EXAFS spectra and Fourier transforms of the soil sample. c,d) Comparison of data obtained for the paddy soil from Taiwan and the fragipan horizon from the Ohio River basin studied by Manceau et al. (2004).

Fig. 16. a) Zn K-edge EXAFS of an homogeneous powder from twenty Fe-Mn and Fe mottles (Zn-Powder spectrum) compared to that of the <0.2 μm soil fraction (Zn-35°). b-c) Comparison of the two previous spectra with the μ-EXAFS spectrum at spot 2 (Zn-2, lithiophorite). Spectral differences are pointed with arrows.

Fig. 17. Zn K-edge EXAFS spectrum from the <0.2 μm soil fraction (Zn-35°) compared to a selection of reference compounds: Zn-sorbed (Zn-sorbed HIM) and Zn-coprecipitated (Zn-copr. HIM) hydroxy-Al interlayered phyllosilicate, Zn-substituted kerolite (ZnKer003, $Zn_{0.03}Mg_{2.97}Si_4O_{10}(OH)_2{\cdot}nH_2O$), natural Zn-containing montmorillonites (SAz-1 and Redhill), and Zn-Al layered double hydroxide (LDH, $Zn_2Al(Kim\ et\ al.)_6[CO_3]_{0.5}$). Kerolite is used as a proxy for the general class of Zn-containing trioctahedral phyllosilicate.

Fig. 18. Polarized EXAFS and Fourier transforms from the <0.2 μm soil fraction and the Redhill montmorillonite reference.

Fig. 19. Inverse Fourier transforms of the first and second RSF peaks, with spectral simulations, for the Zn data at spot 2 (Zn-2), the sample powder (Zn-Powder), the <0.2 μm soil fraction at α

= 35° (Zn-35°), the Redhill montmorillonite (α = 10° and 80°), and the Zn-sorbed hydroxy-Al phyllosilicate (Zn-sorbed HIM).

Table 1. Chemical analysis of the soil exclusive of soft mottles (soil), of four ferruginous mottles (Fe1 to Fe4), and one ferromanganiferous mottle (Fe-Mn).

	Soil	Fe1	Fe2	Fe3	Fe4	Fe-Mn
Al (mg/g)	33.3	18.9	18.0	37.0	43.0	15.6
Fe (mg/g)	6.8	37.7	53.2	71.1	45.1	40.1
Mn (mg/g)	0.2	0.5	0.4	0.3	0.5	44.4
Ti (mg/g)	6.0	5.4	4.9	5.1	5.4	4.1
Mg (mg/g)	3.4	2.8	2.4	2.1	2.4	1.0
K (mg/g)	5.3	4.0	3.9	5.1	7.1	2.2
Na (mg/g)	1.6	1.3	0.9	1.2	1.4	0.8
Ca (mg/g)	0.8	0.3	0.2	0.7	1.0	0.2
P (mg/g)	0.1	0.1	0.2	0.1	0.2	0.2
Ni (mg/kg)	46	50	43	45	49	112
Zn (mg/kg)	42	54	53	56	57	73
Cu (mg/kg)	21	25	28	38	31	32
Co (mg/kg)	9	16	13	12	15	430
Ce (mg/kg)	67	31	16	48	90	159
Pb (mg/kg)	10	28	37	35	36	137
Ba (mg/kg)	424	355	292	291	350	1273

Table 2. EXAFS parameters

Sample	α	O shell			Al shell			Si shell			ΔE	*Rp*	*Ni*	*Nf*
		R (Å)	*CN*	σ^2 (Å^2)	*R* (Å)	*CN*	σ^2 (Å^2)	*R* (Å)	*CN*	σ^2 (Å^2)	(eV)			
Redhill-80°	80°	2.06	5.7[a]	0.008	-	-	-	3.23	8.7[a]	0.009	9.0	16	12	7
Redhill-55°	55°	2.06	5.7[a]	0.008[b]	3.01[c]	3.1[a]	0.010[c]	3.23[b]	8.1[a]	0.009[b]	8.7	12	12	5
Redhill-35°	35°	2.07	6.1	0.008[b]	3.01	3.6	0.010	3.23[b]	5.6	0.009[b]	9.2	19	12	7
Redhill-10°	10°	2.07	6.4[a]	0.008[b]	3.01[c]	4.5[a]	0.010[c]	3.23[b]	3.1[a]	0.009[b]	9.7	21	12	5
Zn-35°	35°	2.08	6.5	0.012	3.06	6.1	0.010	-	-	-	9.8	11	10	7
Zn-Powder	35°	2.08	4.8	0.004	3.06	5.9	0.008	-	-	-	9.5	11	10	7
Zn-copr.	-	2.08	5.5	0.006	3.08	7.1	0.007	-	-	-	10.7	18	14	7

HIM														
Zn-sorbed	-	2.07	5.6	0.009	3.07	5.1	0.009	-	-	-	10.2	13	14	7
HIM														
Zn-2	35°	2.03	5.4	0.003	3.01	7.0	0.005	-	-	-	6.9	15	10	7
Ohio soil	35°	2.07	6.6	0.009	3.01	7.0	0.008	-	-	-	8.7	15	10	7

Ni: Number of independent data points; *Nf*: number of fit parameters. EXAFS structural and electronic parameters were optimized by minimizing the *Rp* parameter defined as sum{|*y*-*yfit*|}/sum{|*y*|}.

[a] effective coordination numbers; [b] fixed to value at $\alpha = 80°$; [c] fixed to value at $\alpha = 35°$; $S_0^2 = 0.80$

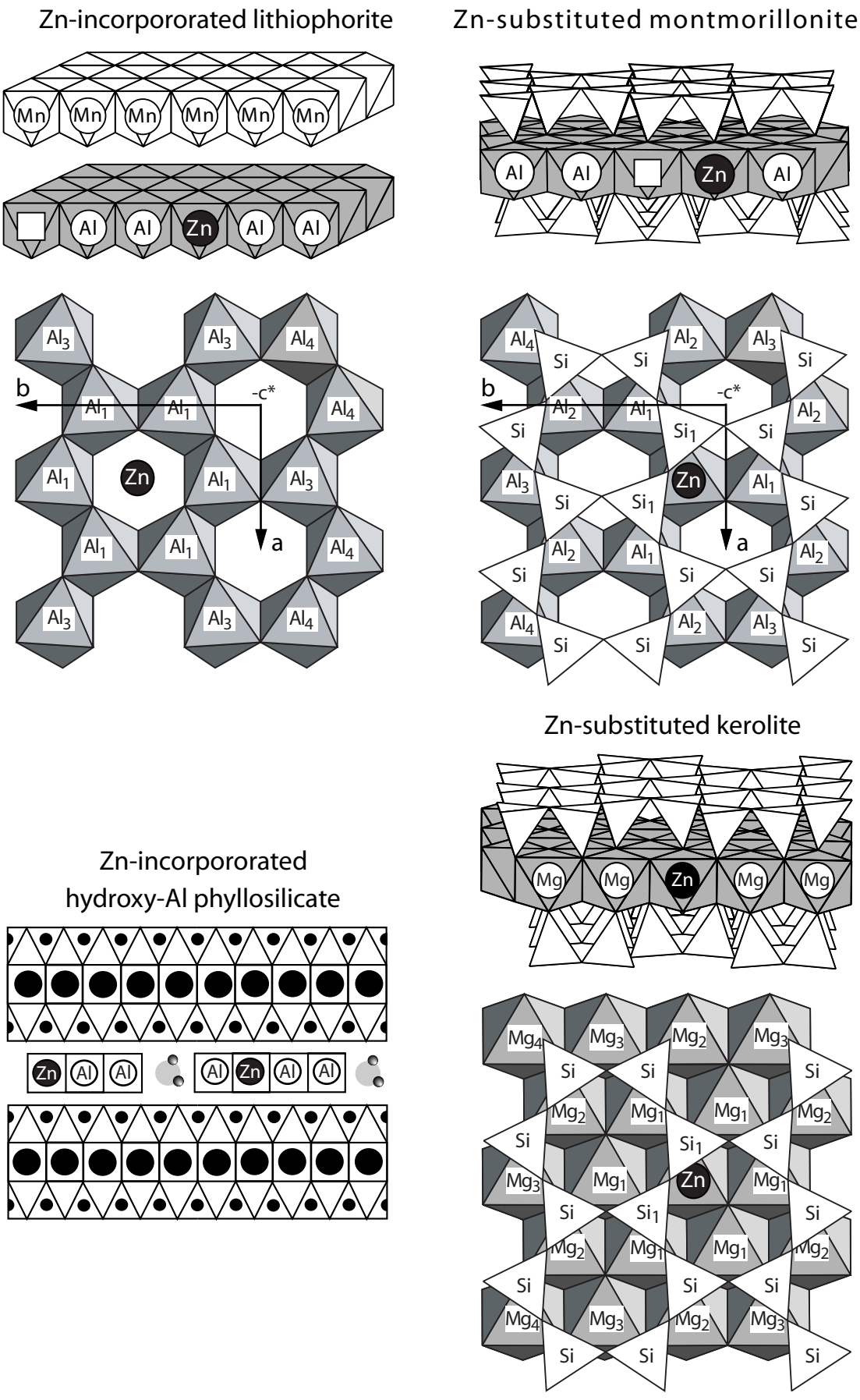

Fig. 1 Manceau et al.

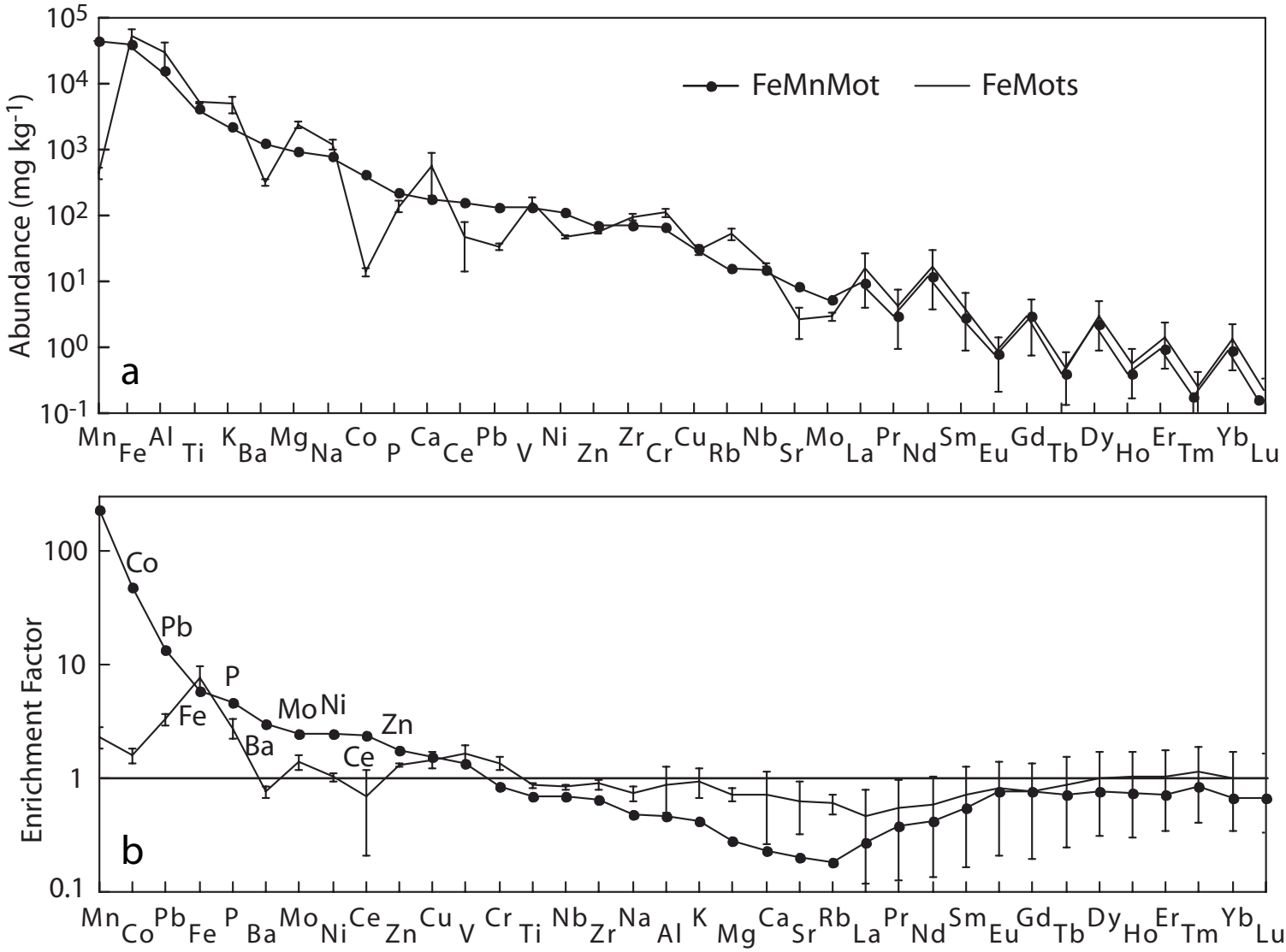

Fig. 2 Manceau et al.

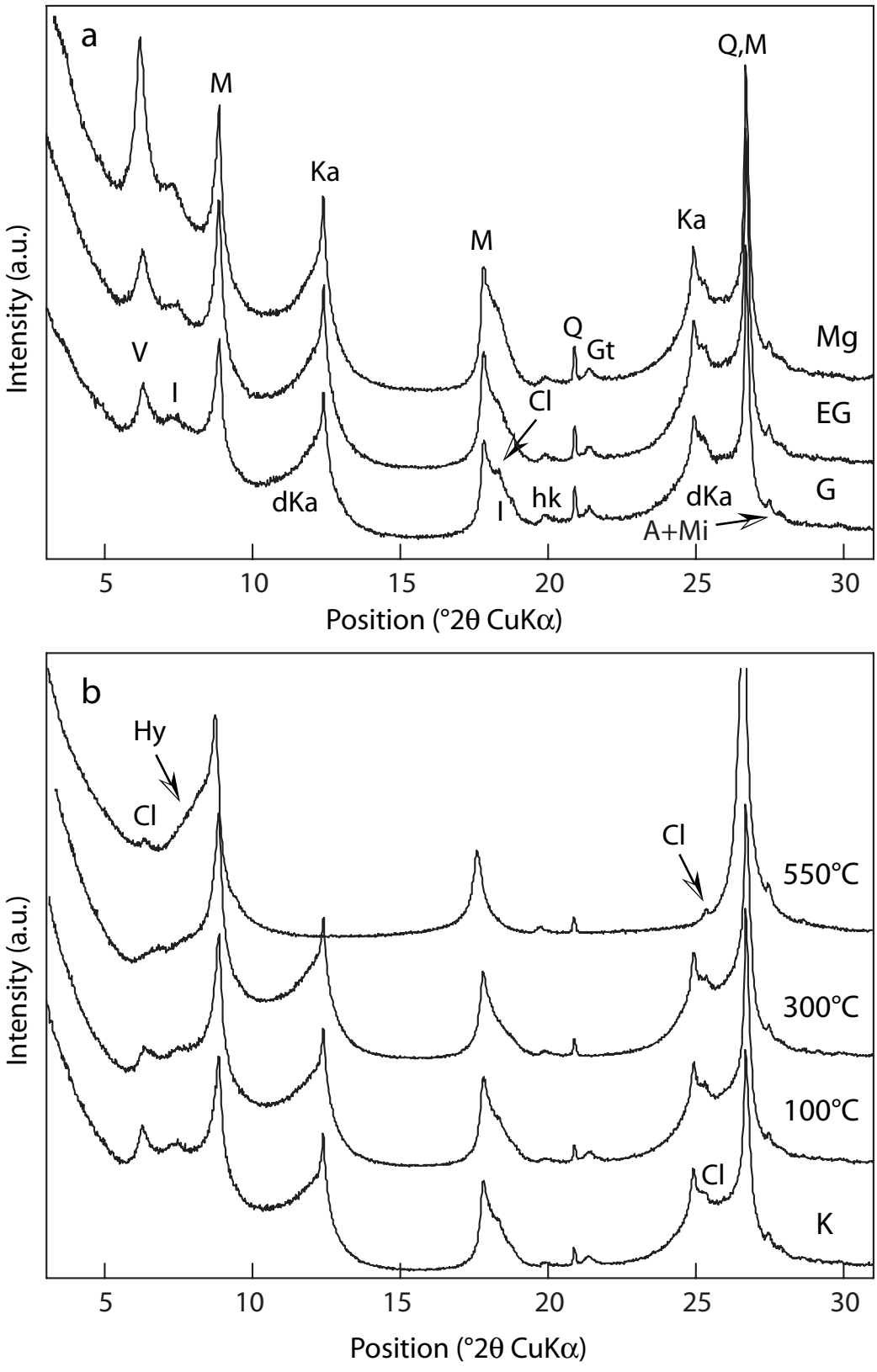

Fig. 3 Manceau et al.

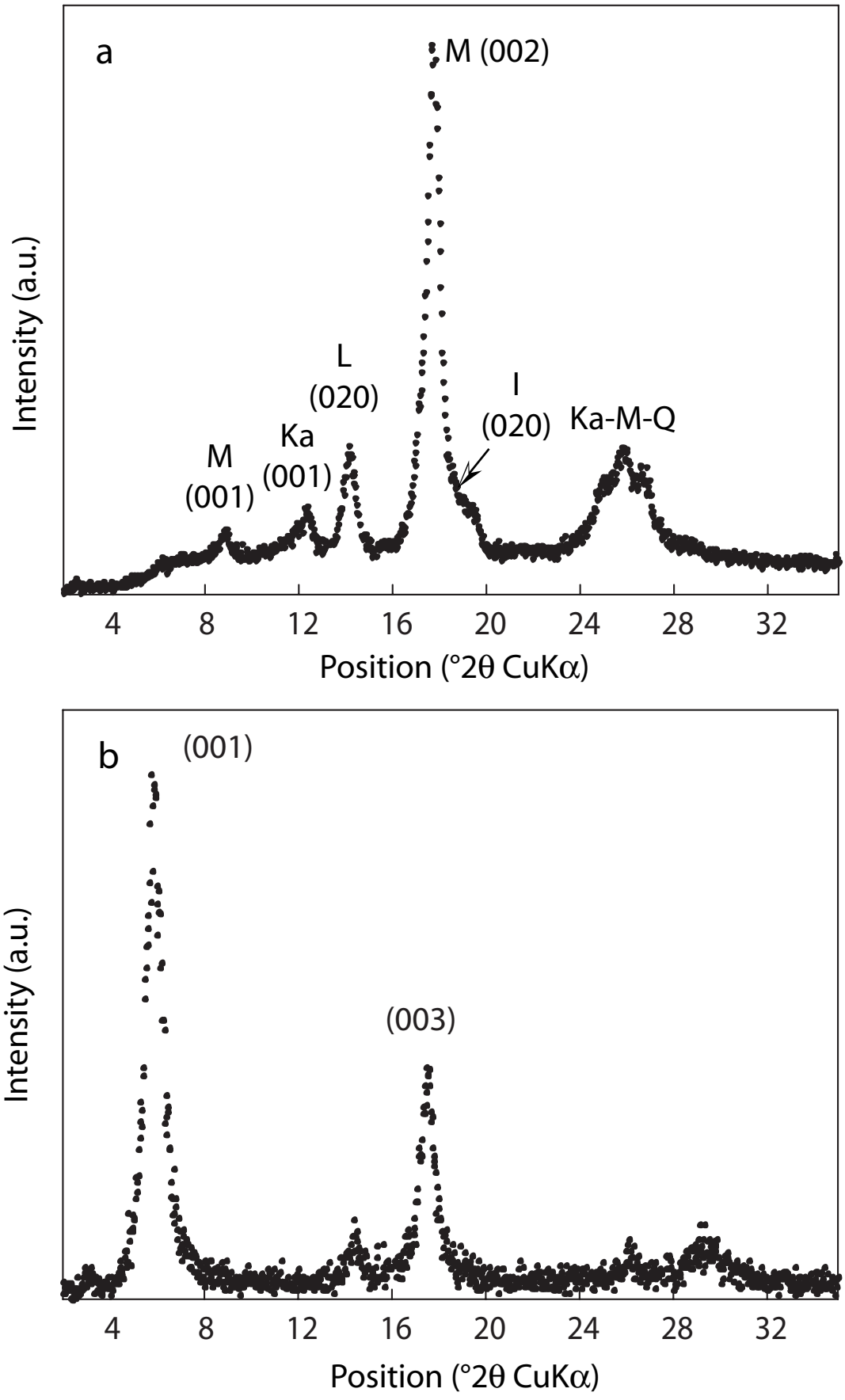

Fig. 4 Manceau et al.

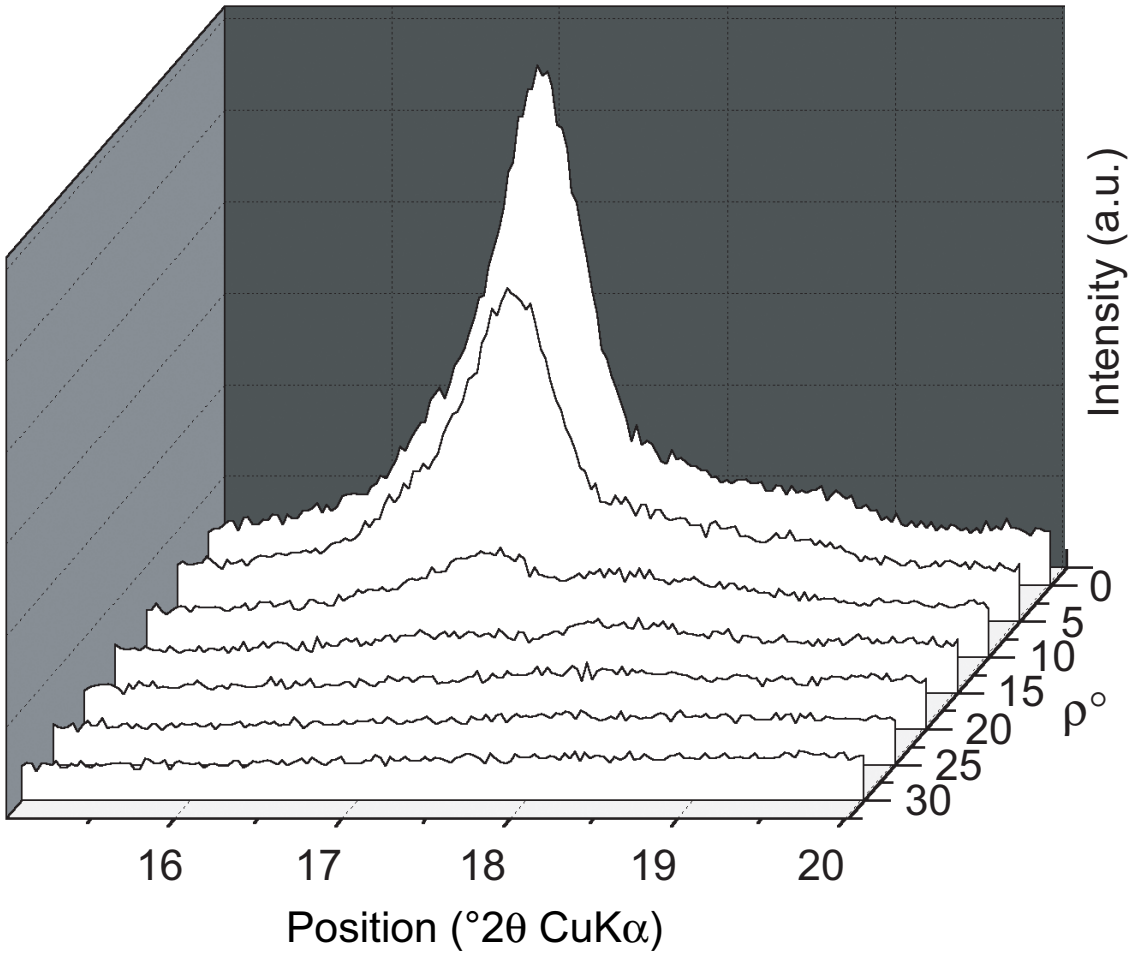

Fig. 5 Manceau et al.

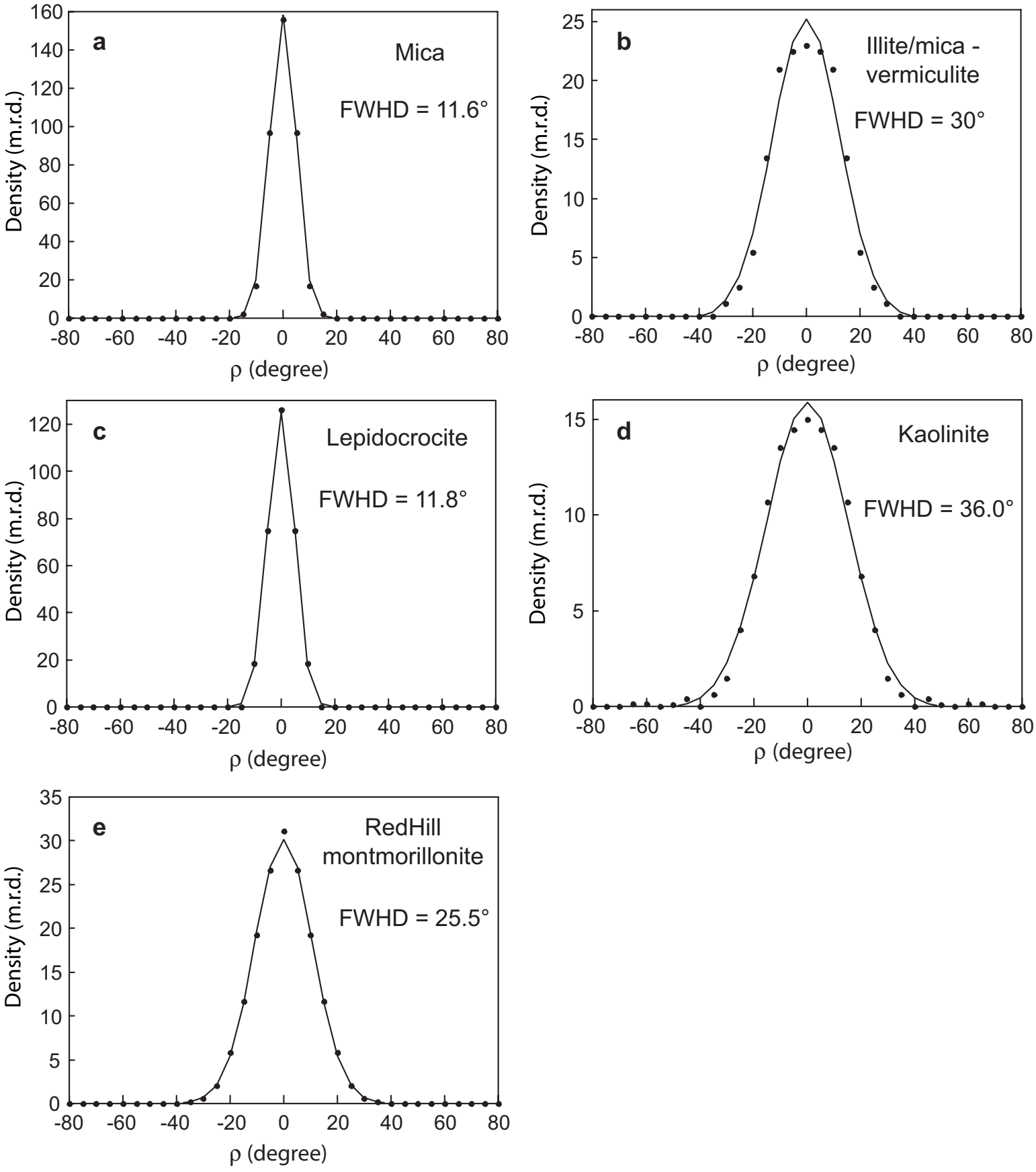

Fig. 6 Manceau et al.

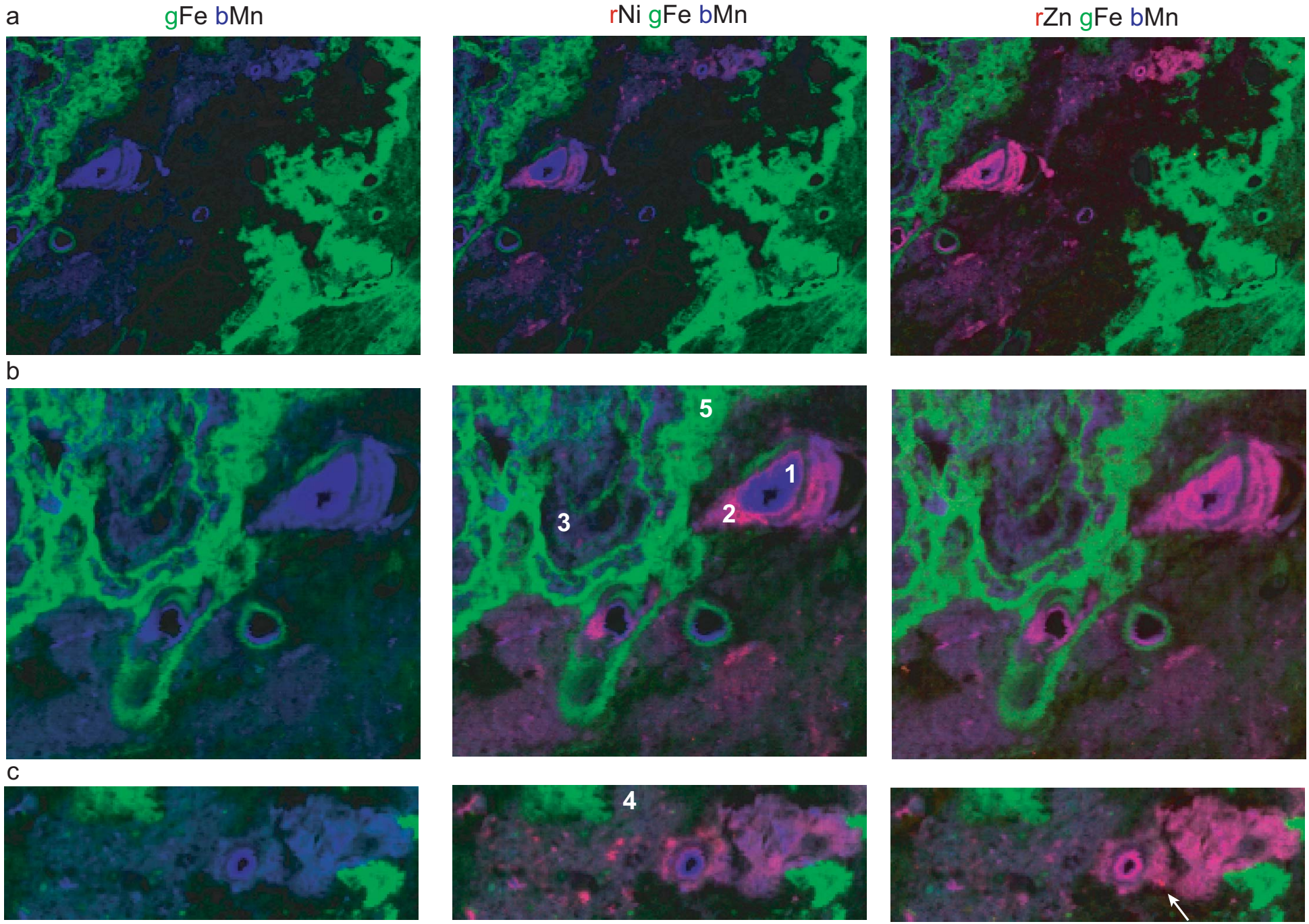

Fig. 7 Manceau et al.

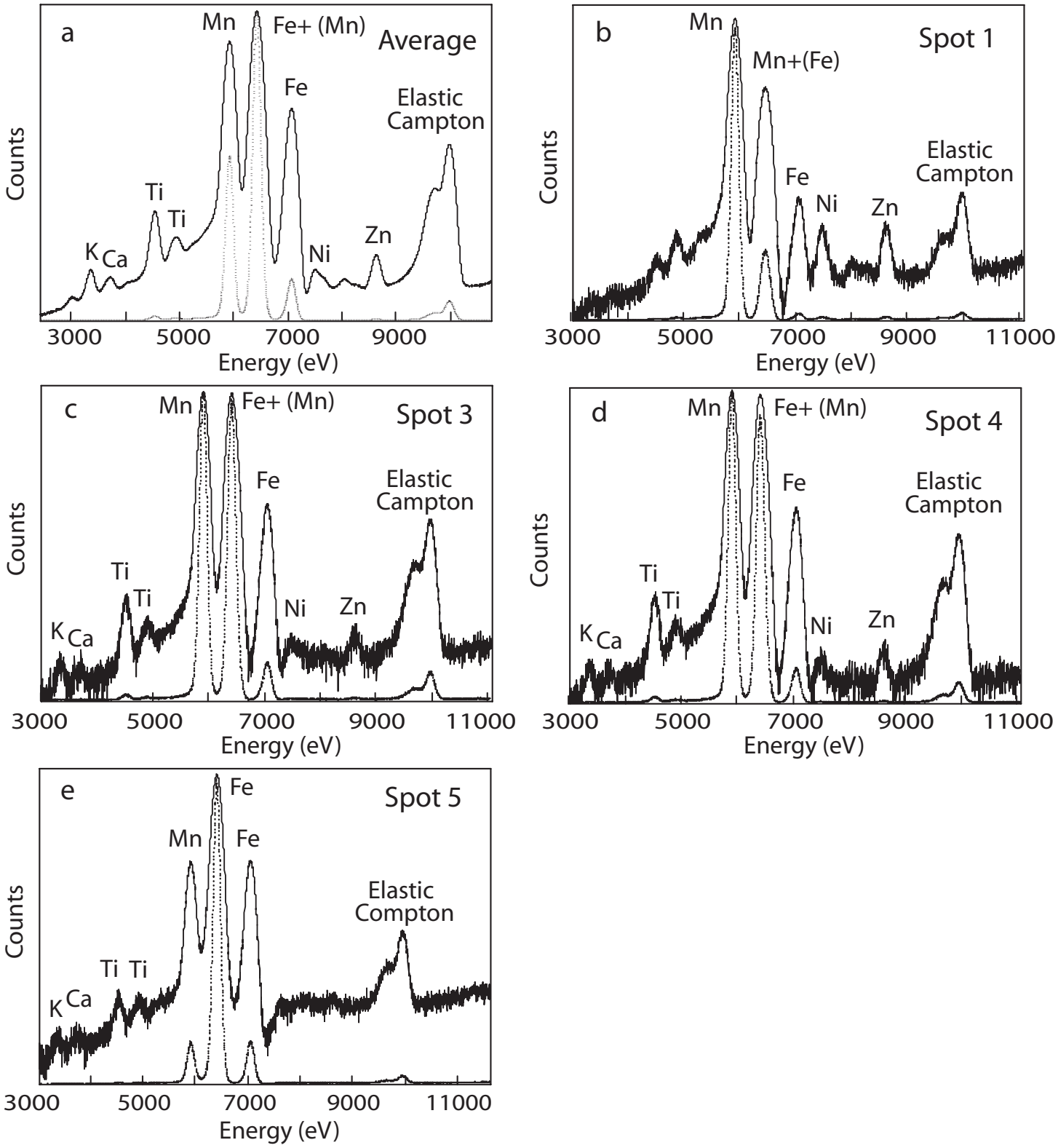

Fig. 8 Manceau et al.

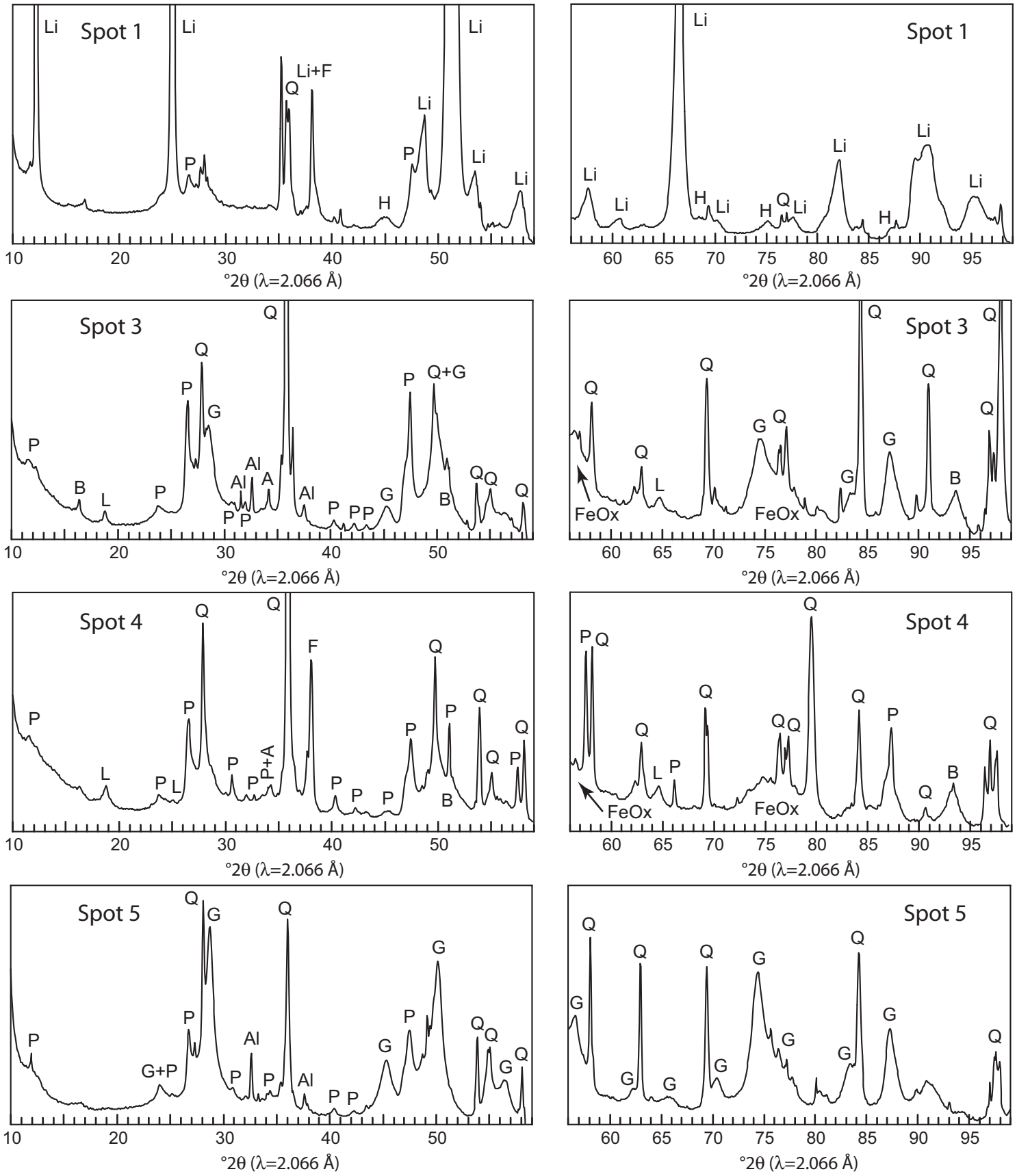

Fig. 9 Manceau et al.

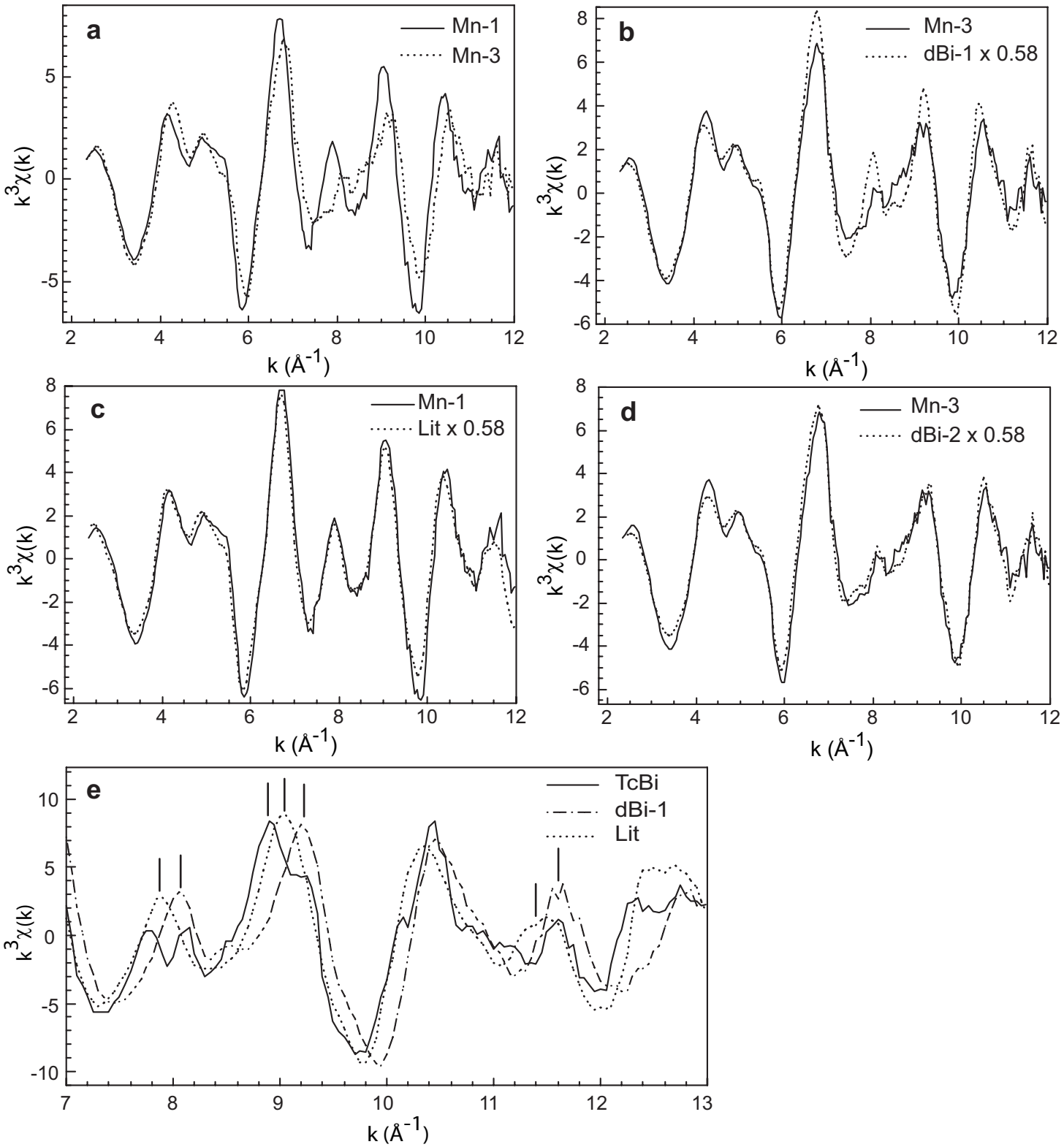

Fig. 10 Manceau et al.

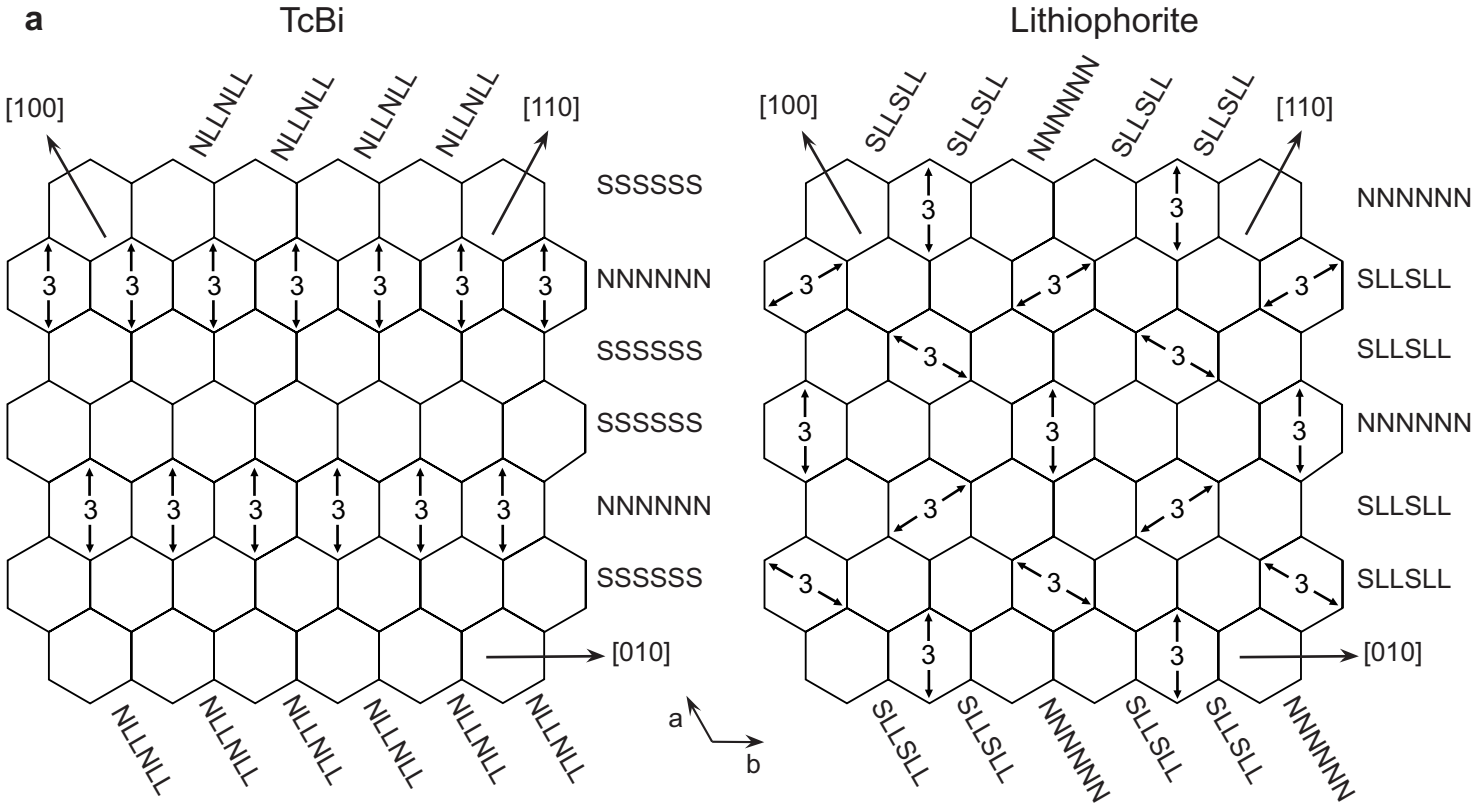

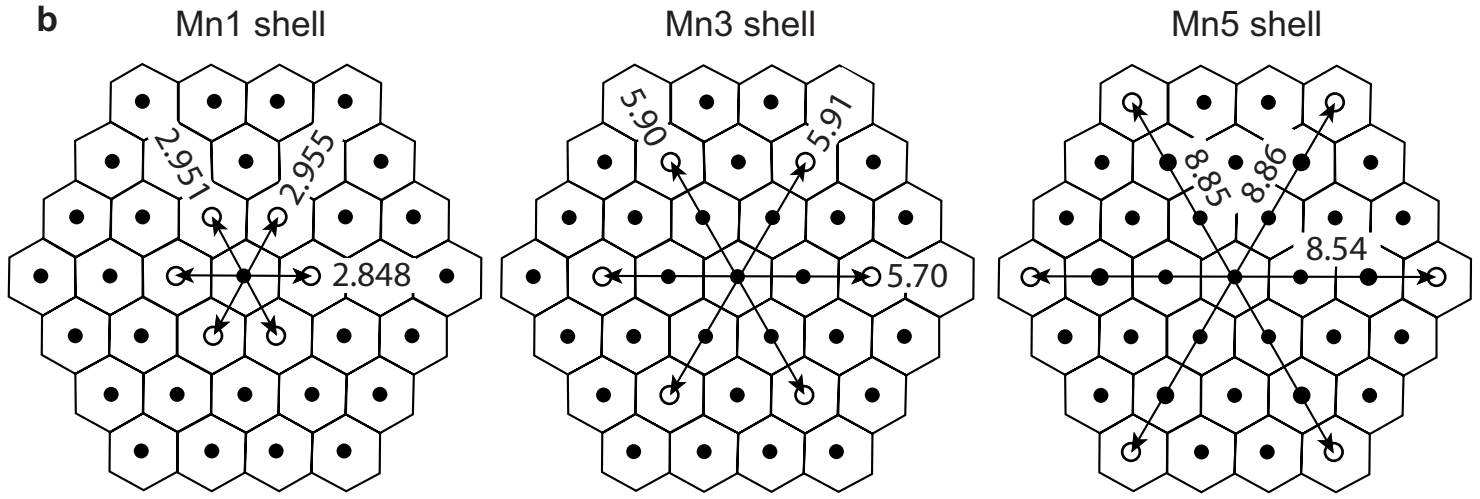

Fig. 11 Manceau et al.

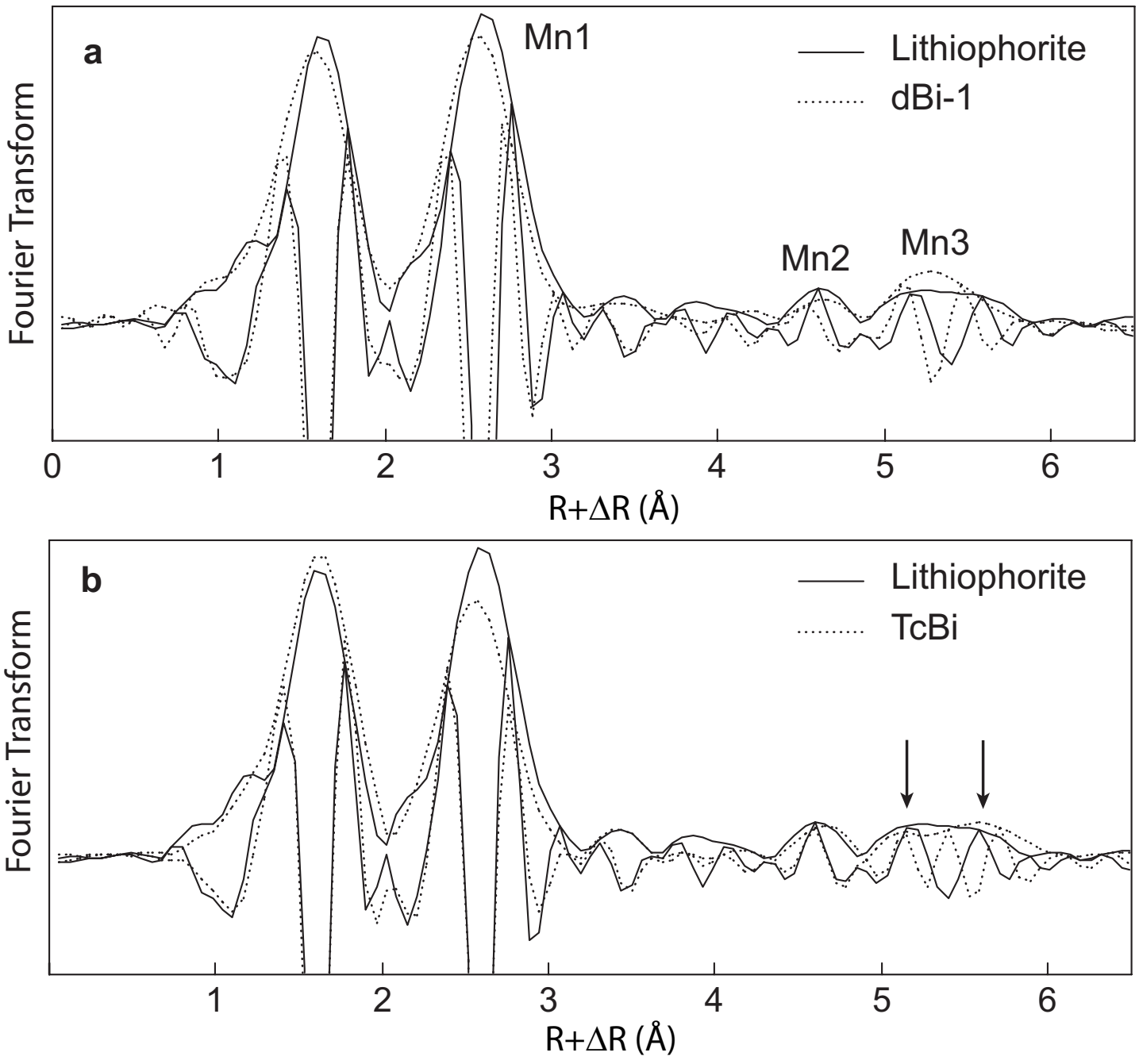

Fig. 12 Manceau et al.

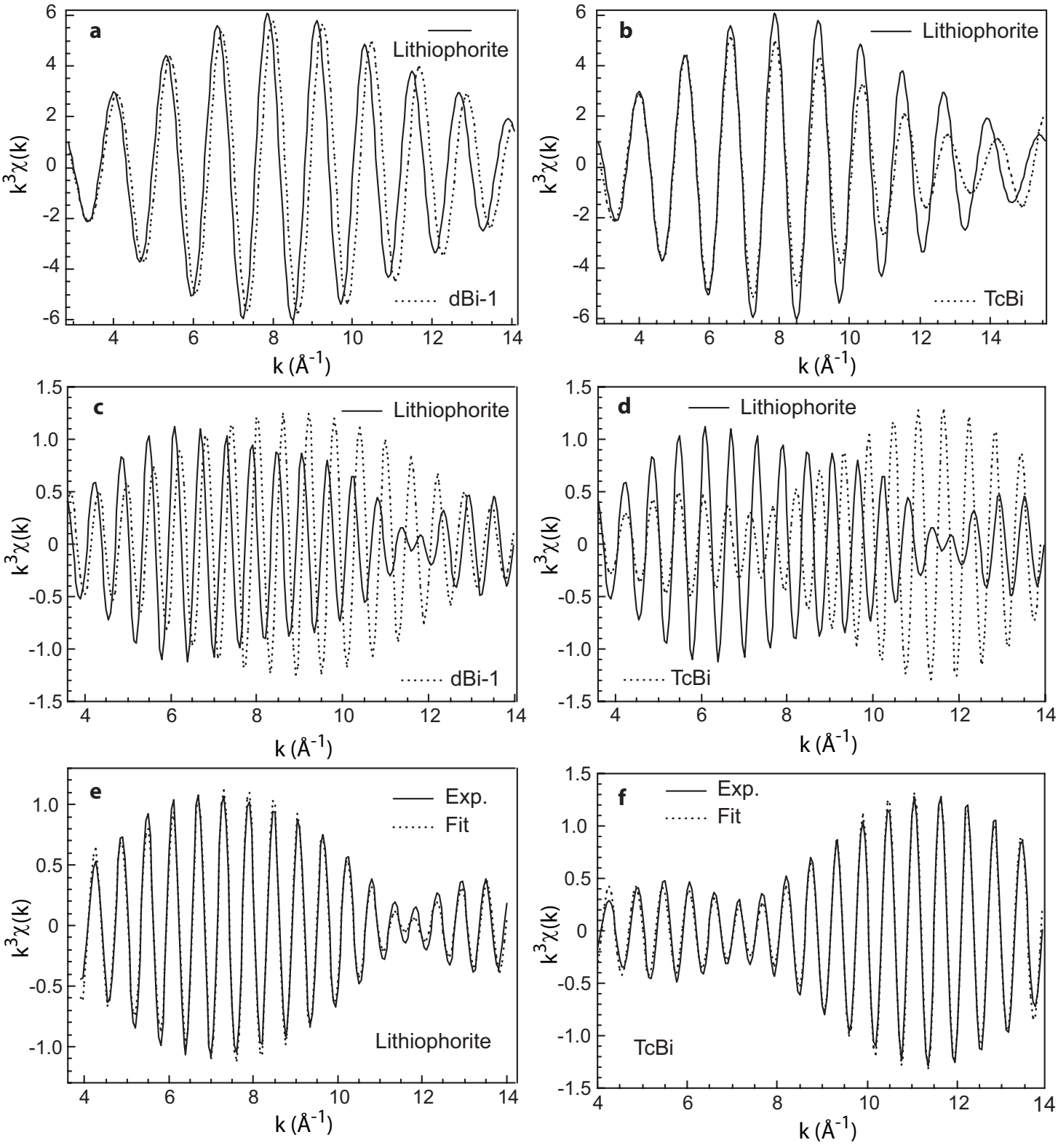

Fig. 13 Manceau et al.

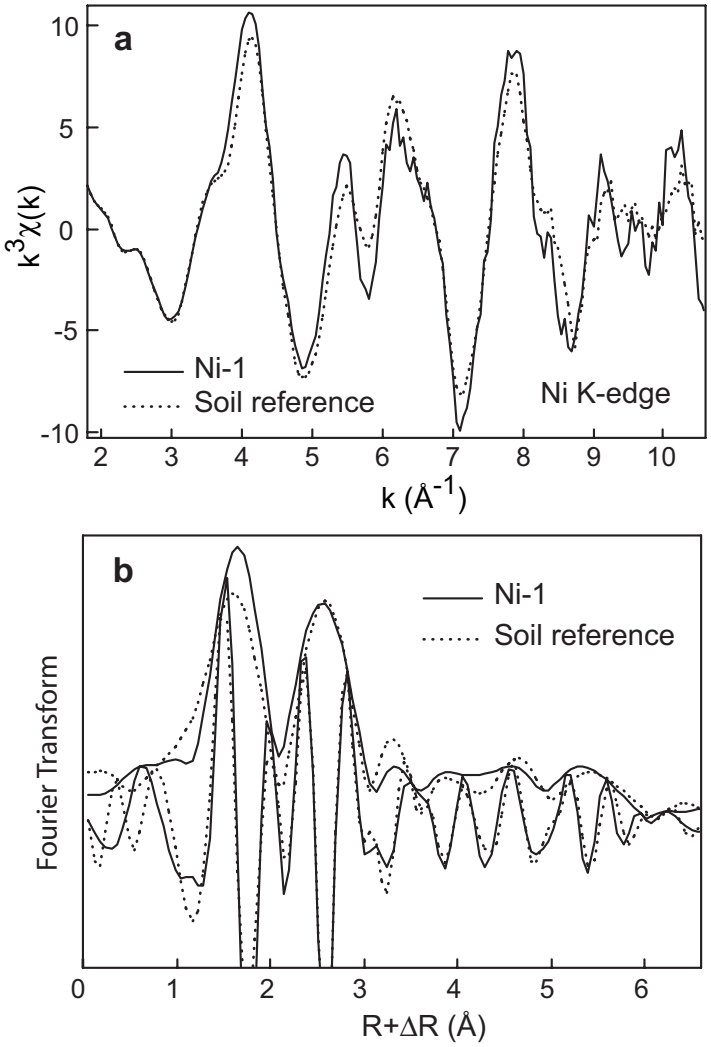

Fig. 14 Manceau et al.

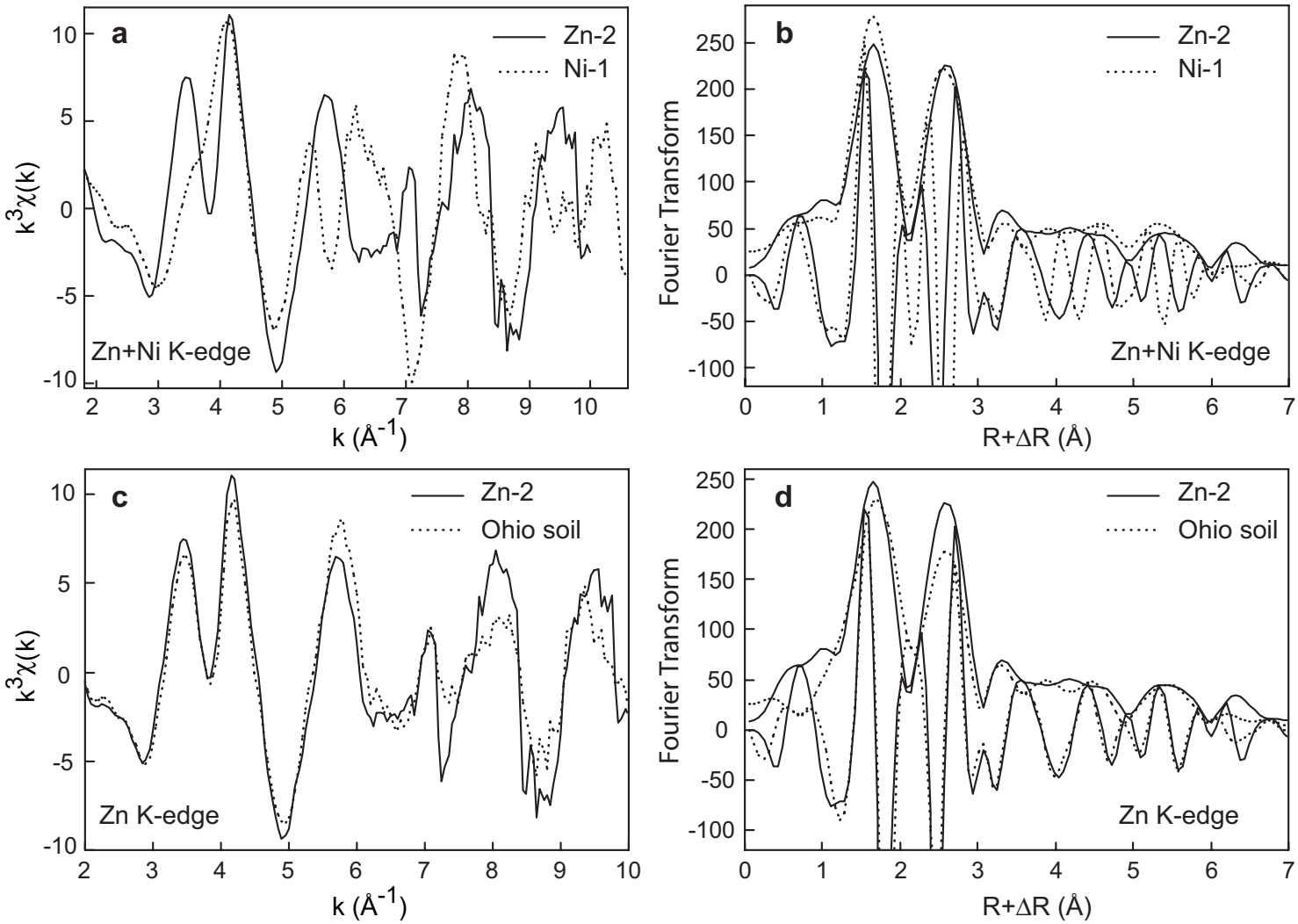

Fig. 15 Manceau et al.

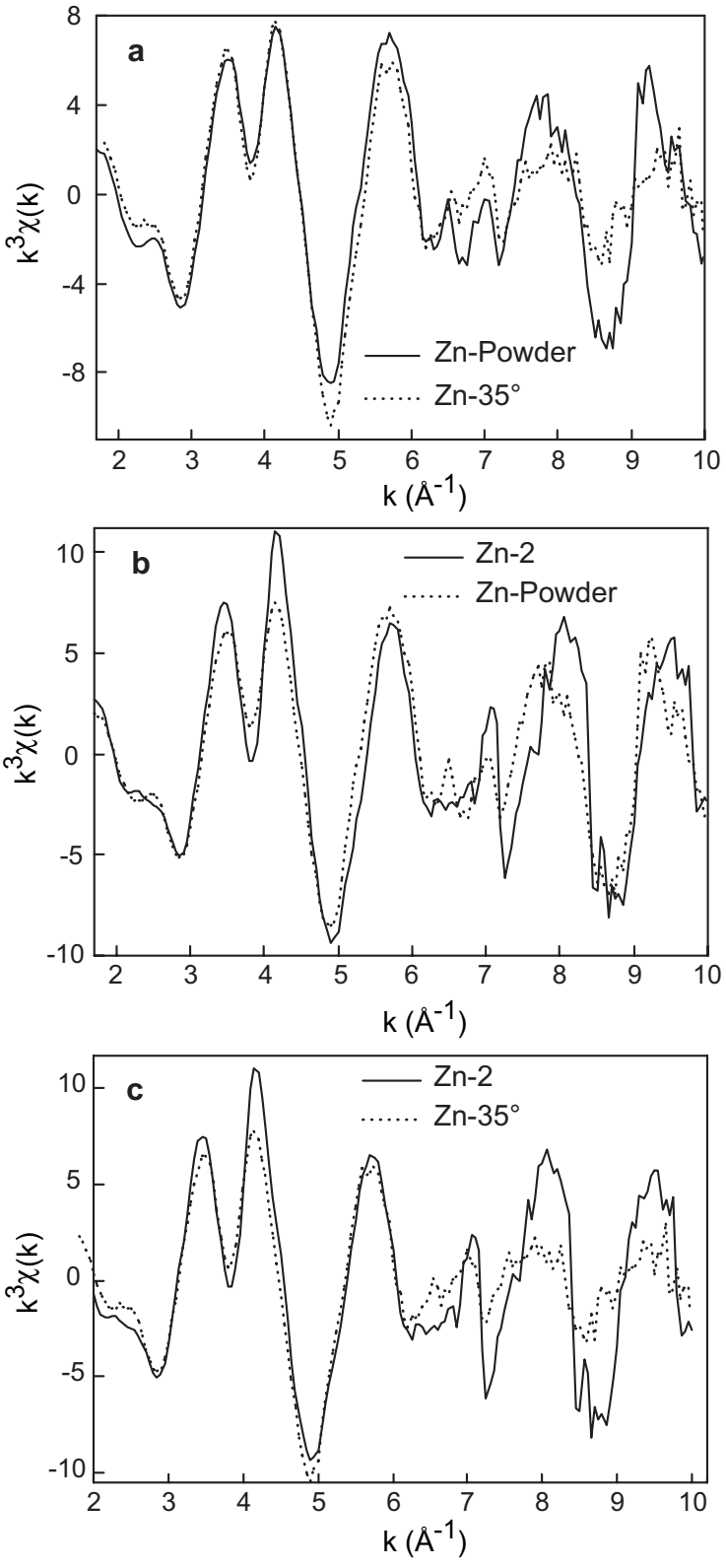

Fig. 16 Manceau et al.

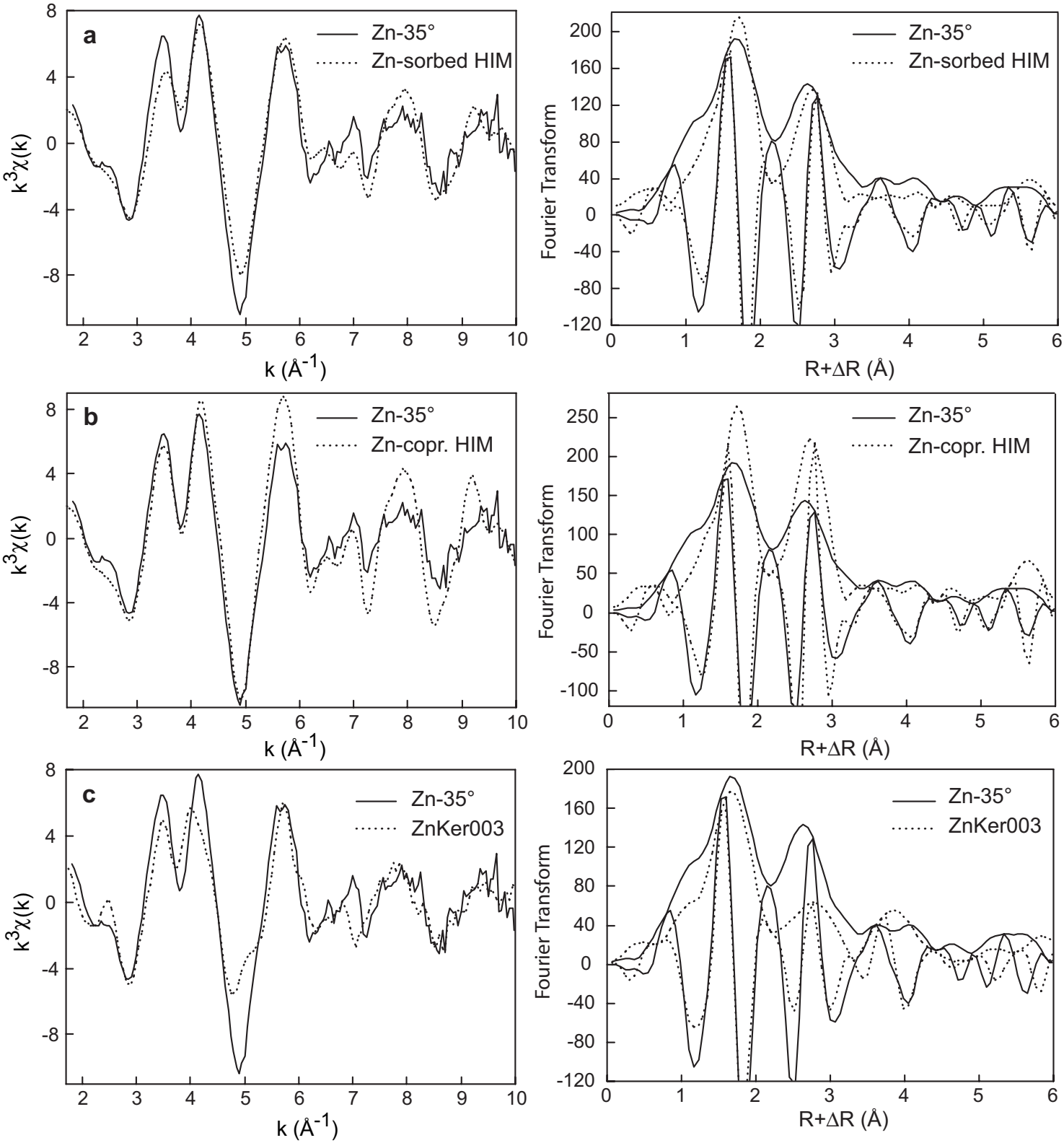

Fig. 17 Manceau et al. (1 of 2)

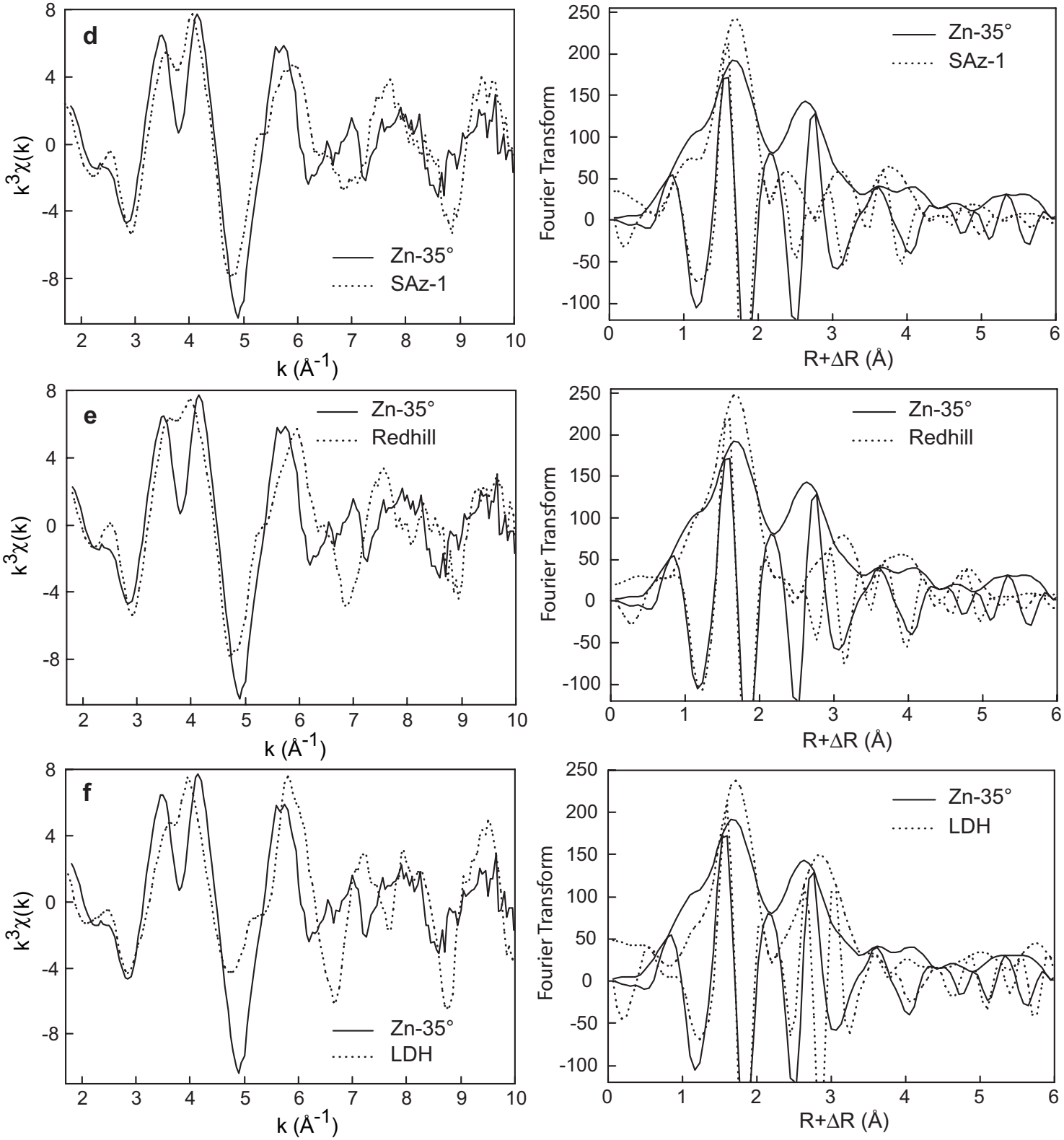

Fig. 17 Manceau et al. (2 of 2)

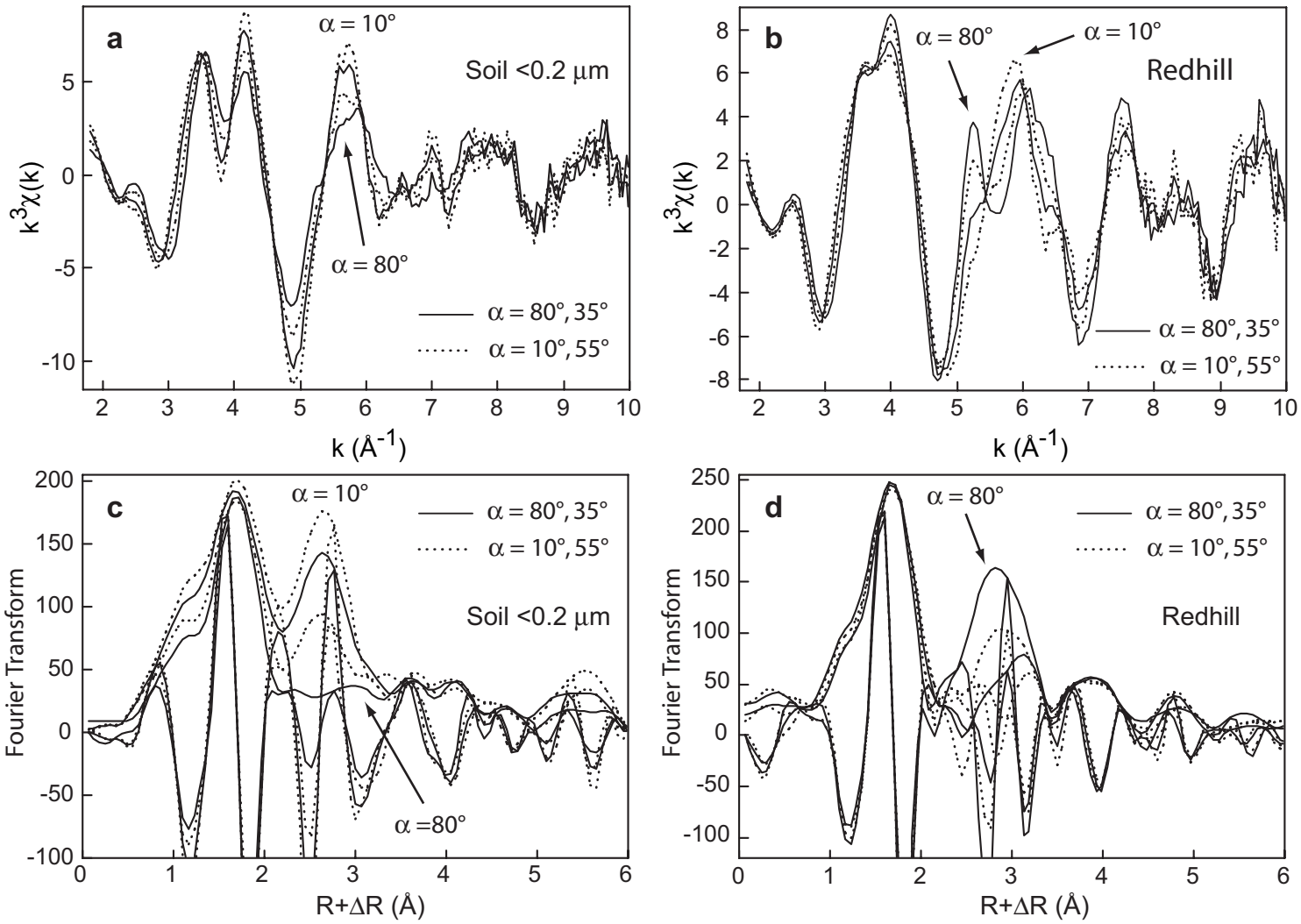

Fig. 18 Manceau et al.

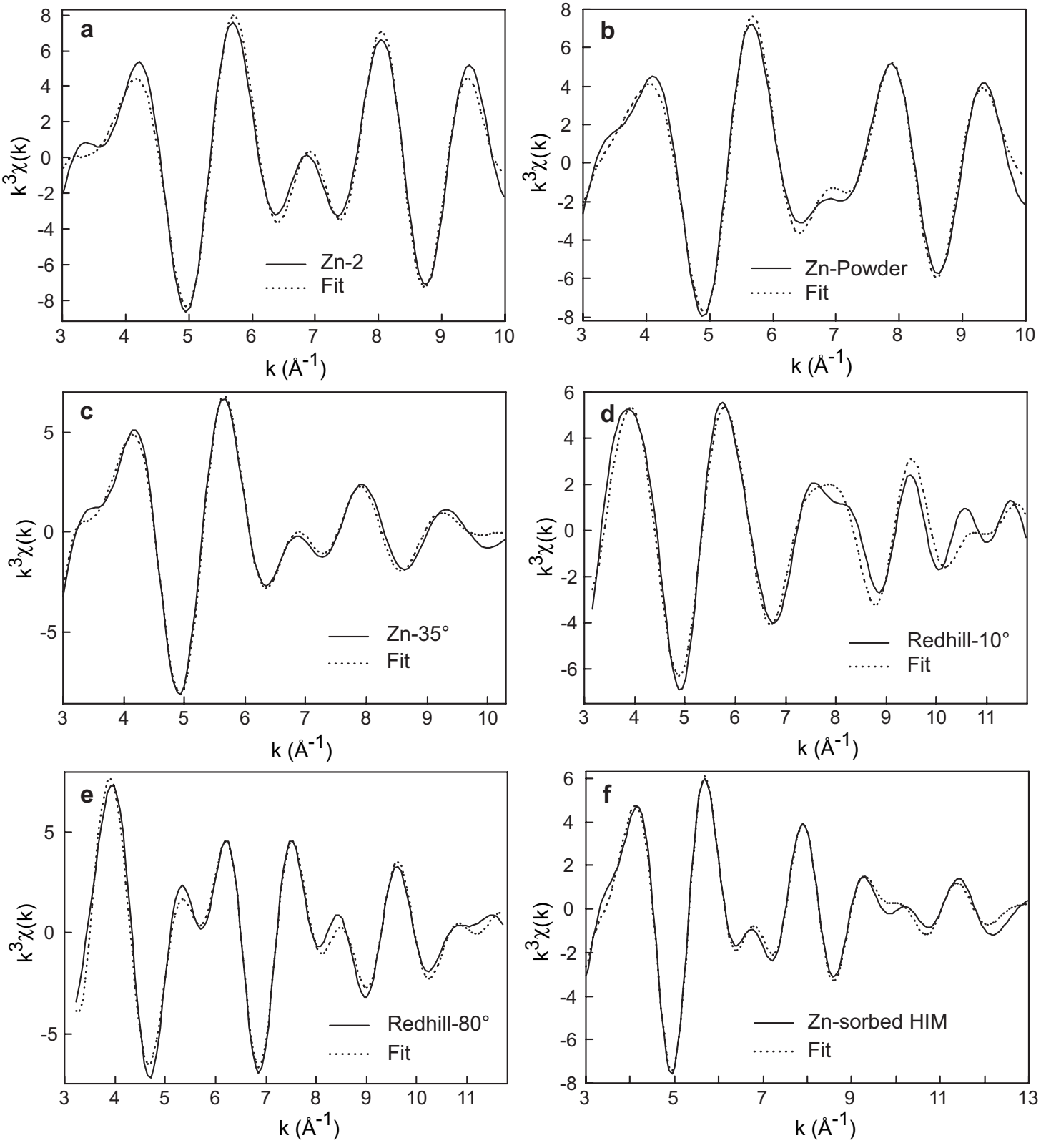

Fig. 19 Manceau et al.